SAND2004-4085
Unlimited Release

Results of Uranium Adsorption/Desorption Experiments and Microanalytical Studies Characterizing Sediment Samples from the Great Miami Aquifer, Fernald DOE Site, Ohio

Submitted by:

Sandia National Laboratories
Albuquerque, NM 87185

Contributing Authors:

Charles R. Bryan[1], Michael Spilde[2], Huifang Xu[2], Carl Schloesslin[3], and Kelsey M. Davis[1]

[1]Center 6800, Sandia National Laboratories, Albuquerque, NM
[2]Department of Earth and Planetary Sciences, University of New Mexico, Albuquerque, NM 87131
[3]Carlsbad Environmental Monitoring & Research Center, Carlsbad, NM 88220

August 2004

This Page Intentionally Left Blank.

Abstract

In Phase I of this study, sediment samples from the uranium contaminant plume in the Great Miami Aquifer, beneath the DOE Fernald site, were analyzed using sequential extraction analysis. This procedure yielded information on how the uranium is partitioned between the minerals in the aquifer sediments and allowed evaluation of the mobility of the uranium—what fraction of the whole is labile, and what fraction is sequestered in mineral structures or by mineral overgrowth and encapsulation. The results of that study showed that whole-rock uranium concentrations in the shallow, uncontaminated samples averaged 1.4 µg/g, the background concentration. Samples from the contaminant plume had higher U concentrations, with a maximum of 5.9 µg/g. Some is present in readily exchangeable sites, loosely sorbed onto mineral surfaces (outer sphere), and possibly in clay interlayers. The largest fraction, however, is associated with carbonate minerals. Much of this is present on the mineral surface and is labile, but a significant fraction, perhaps as much as half, is not readily displaced and may be sequestered in the mineral structure. The amount of uranium associated with amorphous and crystalline iron oxides is minor. The remainder of the uranium, comparable to the amount present in the uncontaminated sediments, is bound in insoluble and nonreactive minerals, and is immobile.

Although little uranium is bound to organic material in the bulk sediment samples, fragments of wood isolated from the sediment contain high concentrations of uranium (up to 41.6 µg/g). Wood in the aquifer probably concentrates uranium through microbially-mediated reduction and precipitation processes.

In Phase II of this study, samples of contaminated sediment have been characterized to further evaluate the relative amounts of labile and fixed uranium present. In addition, wood fragments from the aquifer, concentrated in uranium relative to the surrounding sediment, have been examined to determine the form and location of the uranium in the wood.

Two methods were used to characterize the sediment. In the first, uranium sorption to, and desorption from, contaminated Great Miami Aquifer sediments was evaluated in batch sorption experiments. Contaminated sediment samples were equilibrated with groundwater from the Great Miami Aquifer. Some samples were spiked with small amounts of uranium (80 µg/L); others were equilibrated with unspiked groundwater. In all cases, the uranium concentrations were highest in the initial sample aliquot, and decreased with time. This was apparently due to CO_2 degassing from the groundwater over the course of the experiment—because carbonate strongly complexes uranium, this results in a decrease in U solution concentrations. This is supported by Ca^{+2} concentrations, which also decrease with time, suggesting that calcite precipitated as the solution degassed and the pH rose. Because of the degassing, it is difficult to determine the amount of labile uranium present. If none of the contaminant uranium is fixed, K_d values for the labile fraction of the uranium in the sediment fall in the range of ~9 mL/g. However, the difference in solution concentrations for samples from which differing amounts of uranium had been extracted suggest that a significant amount of the uranium is non-labile, or at least slowly desorbing, resulting in K_d for the mobile fraction of ~3 mL/g.

In the second set of studies, contaminated sediment samples were analyzed using several microanalytical techniques to further evaluate the partitioning of uranium between different sediment minerals, and degree to which some of the uranium may be sequestered by incorporation into mineral lattices or by surface sorption/coprecipitation and mineral overgrowth. Samples were characterized using scanning electron microscopy (SEM), electron microprobe analysis, high resolution transmission electron microscopy (HR-TEM), and secondary ion mass spectrometry (SIMS).

The concentration of uranium in the contaminated sediment is 5.88 μg/g, and concentrations in the oxidized, carbonate-rich groundwater of the contaminant plume are up to a few hundred μg/L—well below solubility limits for uranyl minerals. Thus, uranium phases were not expected in the sediments, and even with Z-contrast imaging by high-resolution transmission electron microscope (HR-TEM), capable of observing clusters of uranium as small as 5-10 atoms, no such phases were found. This strongly suggests that uranium is not present as a discrete phase or coprecipitate, and indicates that uranium is not likely to be sequestered by coprecipitation onto mineral surfaces and mineral overgrowth. However, HR-TEM was useful in characterizing the mineral phases present in the aquifer sediment, and that information is included in this report.

Uranium was observed using secondary ion mass spectrometry (SIMS), in concentrations up to 150 μg/g in the fine (clay-sized) fraction of the sediment. This is not unexpected, as the fine fraction has the highest surface area. Concentrations appeared to be highest in fine materials adhering to larger grain surfaces. Because of the large size of the SIMS ion beam, it was not possible to determine the specific phase in the fine fraction that contained the uranium.

Uranium in wood fragments is associated with pyrite, and is in some cases concentrated in overgrowths on earlier pyrite grains, indicating that sequestration has occurred over the last several decades, since the contaminant plume formed. This suggests that reductive precipitation of a uranium (IV) phase may be an effective method of lowering groundwater U concentrations.

1. Introduction

The Fernald, Ohio DOE site was the location of uranium processing facilities during the cold war and is currently undergoing remediation. Contaminated structures and soil are being removed, and surface cleanup is scheduled to be completed by 2006. A uranium contaminant plume in the aquifer underlying the site is being remediated using pump-and-treat technology. The aquifer remediation project has continued for eleven years, and more than 5000 pounds of uranium have been extracted from over fourteen billion gallons of groundwater to date. Accurately modeling the efficiency of the pump-and-treat remediation, and forecasting remediation completion, requires knowledge of how uranium is adsorbed or partitioned within the aquifer sediments. Uranium that is sorbed onto the surface of sediment components may be able to participate in sorption/desorption reactions. Uranium that is present in individual mineral grains at depths of tens of nanometers or greater is either structurally bound or was present as sorbed or coprecipitated phases that were encapsulated as the coating of the grain grew. Barring changes in pH, Eh, or water chemistry that could result in mineral dissolution, this uranium is sequestered permanently within the grain.

In Phase I of this project, sequential extraction analysis was used to evaluate the partitioning of uranium among mineral phases in the sediment (Bryan et al. 2003). The uranium fractions released in the different steps of the sequential extraction can be used to evaluate how uranium is partitioned among the mineral phases in the sediment, and to estimate the amount of mobile uranium present—that which will participate in transport, and which can be removed by pump-and-treat remediation. This parameter is necessary in order to calculate an accurate partition coefficient, or K_d, for uranium onto the aquifer sediments, and to evaluate remediation goals.

This analysis showed that the majority of the uranium in the sediment is associated with carbonate minerals, and that, while a large fraction is labile (although strongly sorbed, probably as inner-layer complexes), a significant fraction of the carbonate-associated U did not appear to be readily leached. It is possible that some of the uranium was incorporated into the mineral structure, or was coprecipitated and sequestered by mineral overgrowth. Phase II of this study was designed to evaluate the mechanisms of sorption and sequestration, and to determine the actual proportion of labile uranium present to allow more accurate calculation of K_d values.

Lesser amounts of uranium in the sediment are present in readily exchangeable surface sites and clay interlayer sites, or are sorbed to iron oxides/oxyhydroxides.

In the Phase II work, the most contaminated sediment sample identified in Phase I of the study, (from borehole KD33262, depth interval 52.75'–53.75') was used in sorption/desorption experiments and characterized using several microanalytical techniques, including secondary ion mass spectrometry and scanning and transmission electron microscopy, to more thoroughly evaluate the relative proportion of labile and nonlabile uranium present. A second sample, of significantly uranium–enriched wood from the aquifer, was also analyzed. The results of the sorption/desorption experiments confirm that a significant fraction of the uranium in the sediments desorbs only slowly, and may in fact be irreversibly sorbed. Microanalytical characterization of the sediment

sample suggests that the uranium is associated with carbonates, although association with clay phases cannot be ruled out. In the wood samples, uranium is associated with iron sulfide phases.

All sorption experiments were carried out at the Carlsbad Environmental Monitoring & Research Center, a branch of New Mexico State University. The microanalysis work was performed at the University of New Mexico Department of Earth and Planetary Sciences.

2. Sample Descriptions

A complete description of the samples, and of initial sample processing, is given in the final report for Phase I of this project (Bryan et al., 2003). The sediment sample used in the batch sorption and characterization experiments is from borehole KD33262, depth interval 52.75'–53.75'. It was split into separate sieve fractions for Phase I of this project; for this phase, aliquots of the <4 mesh sieve fractions were recombined in proportions equal to their contribution to the total, and the recombined sediment was used in the experiments. The >4 mesh fraction was not used, as this material was so coarse that individual grains could constitute a significant fraction of the sample, decreasing the surface area in the system, and thus biasing the results. The dried, loose sediment was provided to CEMRC for the batch sorption experiments, and to UNM for characterization by microanalysis. UNM also received a polished section of the epoxy-impregnated sediment.

The second sample consisted of loose wood fragments—chips and twigs up to a few centimeters in size—and sediment from borehole KD33298, depth interval 66.0'–66.5', was also provided to UNM. The inorganic portion of this material was somewhat finer-grained than is typical for this aquifer, consisting of sand- and clay-sized material, with few pebbles larger that several mm. A polished section of epoxy-impregnated wood fragments and twigs from this sediment furnished to UNM. An additional sample, of wood fragments from KD33265 (78.0'-78.5') was also provided.

The groundwater used in the sorption experiments was obtained from Fluor Fernald (sample # 53000-0002, sampled 7/30/03), and is from an uncontaminated part of the Great Miami aquifer at the Fernald site. A partial analysis, consisting of the anions, was also provided and is presented in Table 1.

Table 1. Partial Analysis of Groundwater Sample #53000-0002 (provided by Fluor Fernald)

Component	Conc., mg/L
Alkalinity	272.4
SO_4^{2-}	93.5
Cl^-	33.4
NO_3^- as N	<1.0
PO_4^{3-}	<0.1

This Page Intentionally Left Blank

3. Experimental Methods

3.1 Sorption experiments

In order to evaluate the fraction of labile uranium on the contaminated sediments, a series of sorption experiments were carried out. In these experiments, contaminated sediment (KD33262 52.75'-53.75') was equilibrated with groundwater from the Fernald site, and the uranium concentration in solution was monitored over time. To simulate aquifer conditions, a high sediment/groundwater ratio was used. Just enough water was added to saturate the sediment, resulting in a sediment:solution ratio of 35 g:8 mL. Water samples were periodically extracted from the batch systems by use of an Unsaturated Flow Apparatus (UFA), a modified centrifuge. The batch equilibration experiments were carried out in sample containers with bottom ports. At each sampling interval, this container was placed in the UFA, and as much solution as possible was centrifuged out of the sediment. Depending on the set of samples, this was either replaced with fresh groundwater, or a 0.5 mL aliquot was retained, and the remainder returned to the sample.

Three sets of samples were used. In each, the groundwater was spiked with 80 µg/L uranium (a level similar to that present in the groundwater plume), and equilibrated for three weeks, with periodic sampling. One-half milliliter of sample was collected at each sampling. After 21 days, as much of the remaining groundwater as possible was centrifuged out of the sample and collected. Then, a second aliquot of groundwater, containing 30 µg/L U, was added, and the sample was equilibrated for an additional 3 weeks, with periodic sampling. Then, the remaining groundwater was extracted, and a third aliquot of groundwater, containing 20 µg/L U, was added. The sample was equilibrated and sampled for a third and final 3 weeks. The three sample sets had differing sampling intervals—this was to evaluate the potential effect of the changing sediment/water ratio as groundwater samples were extracted. Each set consisted of a pair of duplicate samples spiked with uranium and a pair of unspiked samples. The unspiked samples serve as blanks for the spiked samples and are also used to evaluate the amount of uranium that can be readily stripped from the sediment. With this goal in mind, the sampling strategy was modified for one of each pair of blanks—at each sampling interval, as much groundwater as possible was centrifuged out and retained for analysis, and replaced with fresh groundwater.

The complete experimental matrix is summarized in Table 2. Those batch systems from which 0.5 mL of groundwater was retained at each sampling and the rest reinfused into the sediment (the A-2, Ab-1, B-1, B-2, Bb-1, C-1, C-2, and Cb-1 samples), are hereafter referred to as "reinfused" systems. Those blanks from which all groundwater was extracted at each sampling and replaced with fresh groundwater (the Ab-2, Bb-2, and Cb-2 samples) will be referred to as the "full extraction" systems.

Following collection, each groundwater sample was acidified and diluted, and the composition was measured by Inductively-Coupled-Plasma Mass Spectrometry. In addition to uranium, the water samples were analyzed for Al, Fe, Mn, Mg, Ca, Na, and K to monitor potential changes in water chemistry due to mineral precipitation/dissolution or ion exchange.

Table 2. Experimental Matrix for Batch Sorption Experiments (Sample Sizes are 0.5 ml or "A," for all Remaining Solution).

Day	U added	Set #1				Set #2				Set #3			
		U spiked		Unspiked		U spiked		Unspiked		U spiked		Unspiked	
		*A-1**	A-2	Ab-1	Ab-2	B-1	B-2	Bb-1	Bb-2	C-1	C-2	Cb-1	Cb-2
1	80 µg/L	*0.5*	0.5	0.5	A	0.5	0.5	0.5	A				
2		*0.5*	0.5	0.5	A								
5		*0.5*	0.5	0.5	A	0.5	0.5	0.5	A				
8		*0.5*	0.5	0.5	A								
11		*0.5*	0.5	0.5	A	0.5	0.5	0.5	A	0.5	0.5	0.5	A
14		*0.5*	0.5	0.5	A								
17		*0.5*	0.5	0.5	A	A	A	A	A				
21		*A*	A	A	A					A	A	A	A
1	30 µg/L	*0.5*	0.5	0.5		0.5	0.5	0.5					
2		*0.5*	0.5	0.5									
5		*0.5*	0.5	0.5	A	0.5	0.5	0.5	A				
8		*0.5*	0.5	0.5									
11		*0.5*	0.5	0.5	A	0.5	0.5	0.5	A	0.5	0.5	0.5	A
14		*0.5*	0.5	0.5									
17		*0.5*	0.5	0.5	A	0.5	0.5	0.5	A				
21		*A*	A	A	A	A	A	A	A	A	A	A	A
1	20 µg/L	*0.5*	0.5	0.5		0.5	0.5	0.5					
2		*0.5*	0.5	0.5									
5		*0.5*	0.5	0.5	A	0.5	0.5	0.5	A				
8		*0.5*	0.5	0.5									
11		*0.5*	0.5	0.5	A	0.5	0.5	0.5	A	0.5	0.5	0.5	A
14		*0.5*	0.5	0.5									
17		*0.5*	0.5	0.5	A	A	A	A	A				
21		*A*	A	A						A	A	A	A

* Sample A-1 was inadvertently acidified during the initial spiking. Although the sample was immediately neutralized, the results differ from its duplicate, and data from this batch system have been discarded.

Some changes to the planned experimental matrix were implemented during the course of the experiments. First, sample A-1 was accidentally acidified during the spiking procedure. The sample was immediately neutralized, and the experiment carried out as planned. However, the results for sample A-1 differed from those of its duplicate, A-2, and were not consistent with the results of the other samples. For this reason, the data for sample A-1 were discarded. Second, even with the UFA, it proved impossible to extract all the water out of the sediment samples. Thus, when the experimental matrix called for extraction of all groundwater from the sample, generally ~1 mL of liquid remained in the sediment. The solution volume was brought back up to a total of 8 mL by adding 7 mL of fresh groundwater to the sample.

5034

3.2 Microanalytical Techniques

Several microanalytical techniques were used to evaluate the mineralogical distribution of uranium in the sediments. These include electron microprobe and scanning electron microscope (SEM) element mapping and quantitative elemental analysis using polished, epoxy-impregnated sediment mounts; secondary ion mass spectrometry (SIMS) element mapping of polished sediment mounts and depth profiling of individual grain surfaces; and high-resolution transmission electron microscope (HR-TEM) analysis of clay-sized fine materials and of microtome sections of epoxy-impregnated sediment mounts. Detailed descriptions of these techniques, including sample preparation, instrument calibration, analytical conditions, and detection limits, are presented in Appendix A.

This Page Intentionally Left Blank

4. Results and Discussion

4.1 Sorption experiments

Several different competing processes affect the concentration of uranium in solution in the sorption experiments. First, the kinetics of uranium sorption and desorption are important. Generally, desorption of uranium and other heavy metals follows a typical pattern—some fraction of the contaminant desorbs rapidly, and a second fraction desorbs much more slowly. Characteristically, this leads to an initial jump in the uranium concentration in solution, followed by a continued slow increase over time.

A second effect is related to the removal of samples from the system. As the initial amount of liquid present is just sufficient to saturate the sediments, any removal results in an undersaturated system. If sorption/desorption is occurring under equilibrium conditions, this has no effect on the concentration in solution. However, if continued slow desorption is occurring, the net effect will be to take up the released uranium into a smaller volume of solution, leading to a more rapid rise in solution concentration than would be seen in a system with a constant solution volume. It was in an attempt to deconvolve these two affects that different samples were sampled on different sampling intervals—those samples sampled frequently provide resolution in the desorption curve, while those sampled less frequently allow evaluation of the importance of the changing water/rock ratio.

For those samples in which the entire solution was collected at every sampling interval, another effect is important. In these samples, a significant fraction of uranium is removed from the system at each sampling interval. The total uranium present in the system decreases, and it is expected that the most readily leachable uranium will be removed first. Thus, in these samples, one would expect to see a decrease in the solution concentration of uranium with each sampling interval, and a slower build-up between sampling intervals. This effect should not be important in the samples from which only 0.5 mL of sample was collected at each sampling interval, as too little uranium is removed to be significant.

An enormous amount of data was collected by analysis of the groundwater samples collected during the batch sorption experiments. The data is presented in full in Appendix 1. The uranium data are presented in Table 3, and summarized in Figure 1. Results are unexpected: for all samples, the concentration of uranium in solution decreases with time. In addition, for the re-infused samples, the uranium concentration in solution rebounded when fresh solution was added at the beginning the subsequent phases (more than would be expected from the low-concentration spike).

It is reasonable for the uranium concentration to decrease with successive leachings in the full-extraction samples, as a significant amount of uranium (on the order of 0.5 to 1.5% of the total) was removed at each extraction. However, only 1–2% of the uranium was removed from the reinfused samples over the entire suite of extractions. This is far too little to explain the observed drop in concentration. In fact, uranium concentrations in the reinfused samples actually drop more rapidly than in the successive full-extraction samples, even though much less uranium is removed in each leach step. This is

inconsistent with any of the predicted trends, and suggests that the composition of the groundwater is changing with time, such that more uranium is partitioning onto the solid phases (i.e., the K_d is increasing). It seems likely that the carbonate-charged groundwater degassed over the course of the experiment. Because carbonate strongly complexes uranium, degassing results in lower solution concentrations. Alternatively, degassing and the associated rise in pH may have caused changes in the stochiometry of the stable uranyl solution species or sorbed complex, changing the K_d. This results in less uranium partitioning into the liquid phase. The groundwater sample was refrigerated prior to the start of the experiment to minimize degassing, but through an oversight, was left on the table-top once the experiment was initiated. Thus, it was stored at room temperature and periodically sampled over the 60-day duration of the experiment. The increase in headspace as water was periodically removed from the bottle may have also encouraged degassing.

This degassing apparently occurred over two time scales. First, the groundwater degassed slowly on the table-top, over the 60-day course of the experiment. Second, the liquid apparently degassed much more aggressively when it was centrifuged out of the

Table 3. Measured uranium concentrations in the batch systems.

	Cum. Days Elapsed	U conc., µg/L	Volume, mL	Aliquot kept, mL	Cum. U removed[1], ng	Cum. U removed[1], %	(U on solid - bkg), ng/g	K_d[2]
				A-2				
80 µg/L U added	1	327.8	8.0	0.50	0.0	0.0	4428	13.5
	2	316.8	7.5	0.50	163.9	0.1	4430	14.0
	5	294.6	7.0	0.50	322.3	0.1	4434	15.0
	8	270.4	6.5	0.50	469.6	0.2	4438	16.4
	11	244.9	6.0	0.50	604.8	0.3	4442	18.1
	14	235.9	5.5	0.50	727.3	0.3	4444	18.8
	17	192.7	5.0	0.50	845.2	0.4	4449	23.1
	21	182.8	4.5	2.13	941.5	0.4	4450	24.3
30 µg/L U added	22	312.2	8.0	0.50	1330.8	0.6	4402	14.1
	23	279.4	7.5	0.50	1486.9	0.7	4408	15.8
	26	200.7	7.0	0.50	1626.6	0.7	4423	22.0
	29	191.1	6.5	0.50	1726.9	0.8	4424	23.2
	32	179.8	6.0	0.50	1822.5	0.8	4426	24.6
	35	164.1	5.5	0.50	1912.4	0.9	4428	27.0
	38	168.9	5.0	0.50	1994.4	0.9	4428	26.2
	42	151.4	4.5	1.69	2078.9	0.9	4430	29.3
20 µg/L U added	43	225.5	8.0	0.50	2334.4	1.0	4397	19.5
	44	213.1	7.5	0.50	2447.2	1.1	4400	20.6
	47	184.0	7.0	0.50	2553.7	1.1	4405	23.9
	50	181.8	6.5	0.50	2645.7	1.2	4405	24.2
	53	166.4	6.0	0.50	2736.6	1.2	4408	26.5
	56	157.2	5.5	0.50	2819.8	1.3	4409	28.0
	59	125.5	5.0	0.50	2898.4	1.3	4413	35.2
	63	130.5	4.5	1.87	2961.1	1.3	4413	33.8

Table 3. Continued

	Cum. Days Elapsed	U conc., µg/L	Volume, mL	Aliquot kept, mL	Cum. U removed[1], ng	Cum. U removed[1], %	(U on solid - bkg), ng/g	K_d[2]
				Ab-1				
No U added	1	371.8	8.0	0.5	0.0	0.0	4402	11.8
	2	312.9	7.5	0.5	185.9	0.1	4413	14.1
	5	301.4	7.0	0.5	342.3	0.2	4415	14.6
	8	263.8	6.5	0.5	493.1	0.2	4422	16.8
	11	253.7	6.0	0.5	625.0	0.3	4423	17.4
	14	241.3	5.5	0.5	751.8	0.3	4425	18.3
	17	158.0	5.0	0.5	872.5	0.4	4436	28.1
	21	118.5	4.5	2.4	951.5	0.4	4441	37.5
	22	304.6	8.0	0.5	1230.5	0.6	4383	14.4
	23	243.0	7.5	0.5	1382.8	0.6	4396	18.1
	26	197.6	7.0	0.5	1504.4	0.7	4404	22.3
	29	188.2	6.5	0.5	1603.2	0.7	4406	23.4
	32	174.9	6.0	0.5	1697.2	0.8	4408	25.2
	35	166.8	5.5	0.5	1784.7	0.8	4409	26.4
	38	168.5	5.0	0.5	1868.1	0.8	4409	26.2
	42	119.3	4.5	1.7	1952.4	0.9	4414	37.0
	43	226.6	8.0	0.5	2160.1	1.0	4375	19.3
	44	198.8	7.5	0.5	2273.4	1.0	4381	22.0
	47	176.3	7.0	0.5	2372.8	1.1	4385	24.9
	50	174.7	6.5	0.5	2461.0	1.1	4385	25.1
	53	163.6	6.0	0.5	2548.3	1.1	4387	26.8
	56	129.4	5.5	0.5	2630.1	1.2	4392	34.0
	59	99.6	5.0	0.5	2694.8	1.2	4396	44.1
	63	91.6	4.5	1.5	2744.6	1.2	4397	48.0
				Ab-2				
No U added	1	365.5	8.0	7.176	0.0	0.0	4403	12.0
	2	317.1	8.0	7.026	2622.6	1.2	4344	13.7
	5	377.6	8.0	6.922	4850.6	2.2	4273	11.3
	8	332.9	8.0	6.261	7464.4	3.3	4213	12.7
	11	310.5	8.0	5.832	9548.8	4.3	4163	13.4
	14	263.1	8.0	5.865	11359.5	5.1	4126	15.7
	17	218.2	8.0	5.407	12902.6	5.8	4095	18.8
	21	303.9	8.0	5.938	14082.4	6.3	4045	13.3
	26	274.5	8.0	6.791	15887.2	7.1	4004	14.6
	32	250.7	8.0	6.284	17751.1	7.9	3960	15.8
	38	212.7	8.0	5.990	19326.2	8.6	3927	18.5
	42	178.2	8.0	5.814	20600.3	9.2	3900	21.9
	47	189.8	8.0	6.867	21636.6	9.7	3871	20.4
	53	182.7	8.0	6.719	22940.1	10.3	3838	21.0
	59	167.8	8.0	6.465	24167.6	10.8	3809	22.7

Table 3, Continued.

	Cum. Days Elapsed	U conc., µg/L	Volume, mL	Aliquot kept, mL	Cum. U removed[1], ng	Cum. U removed[1], %	(U on solid - bkg), ng/g	K_d[2]
				B-1				
80 µg/L U added	1	376.0	8.0	0.50	0.0	0.0	4418	11.7
	5	362.1	7.5	0.50	188.0	0.1	4420	12.2
	11	320.0	7.0	0.50	369.1	0.2	4428	13.8
	17	264.5	6.5	4.92	529.1	0.2	4438	16.8
30 µg/L U added	22	342.6	8.0	0.5	1829.7	0.8	4382	12.8
	26	271.1	7.5	0.5	2001.0	0.9	4396	16.2
	32	239.6	7.0	0.5	2136.6	1.0	4402	18.4
	38	244.3	6.5	0.5	2256.4	1.0	4401	18.0
	42	247.8	6.0	4.21	2378.5	1.1	4401	17.8
20 µg/L U added	43	256.2	8.0	0.5	3422.1	1.5	4362	17.0
	47	247.3	7.5	0.5	3550.2	1.6	4364	17.6
	53	248.9	7.0	0.5	3673.9	1.6	4364	17.5
	59	244.3	6.5	4.71	3798.3	1.7	4364	17.9
				B-2				
80 µg/L U added	1	387.1	8.0	0.5	0.0	0.0	4415	11.4
	5	372.7	7.5	0.5	193.6	0.1	4418	11.9
	11	335.1	7.0	0.5	379.9	0.2	4425	13.2
	17	267.1	6.5	4.7	547.5	0.2	4437	16.6
30 µg/L U added	22	314.2	8.0	0.5	1790.4	0.8	4389	14.0
	26	263.5	7.5	0.5	1947.5	0.9	4399	16.7
	32	230.3	7.0	0.5	2079.3	0.9	4405	19.1
	38	224.3	6.5	0.5	2194.5	1.0	4406	19.6
	42	170.1	6.0	3.8	2306.6	1.0	4415	25.9
20 µg/L U added	43	242.0	8.0	0.5	2946.1	1.3	4378	18.1
	47	237.4	7.5	0.5	3067.0	1.4	4378	18.4
	53	228.3	7.0	0.5	3185.7	1.4	4380	19.2
	59	187.5	6.5	4.3	3299.9	1.5	4387	23.4

Table 3, Continued.

	Cum. Days Elapsed	U conc., µg/L	Volume, mL	Aliquot kept, mL	Cum. U removed[1], ng	Cum. U removed[1], %	(U on solid - bkg), ng/g	K_d[2]
				Bb-1				
No U added	1	406.6	8.0	0.50	0.0	0.0	4394	10.8
	5	357.9	7.5	0.50	203.3	0.1	4404	12.3
	11	318.9	7.0	0.50	382.2	0.2	4411	13.8
	17	256.3	6.5	4.68	541.7	0.2	4422	17.3
	22	302.7	8.0	0.50	1741.0	0.8	4370	14.4
	26	259.3	7.5	0.50	1892.4	0.8	4379	16.9
	32	198.3	7.0	0.50	2022.0	0.9	4390	22.1
	38	188.1	6.5	0.50	2121.2	0.9	4392	23.3
	42	191.7	6.0	3.83	2215.2	1.0	4391	22.9
	43	232.8	8.0	0.50	2949.5	1.3	4353	18.7
	47	190.0	7.5	0.50	3065.9	1.4	4362	23.0
	53	182.1	7.0	0.50	3160.9	1.4	4363	24.0
	59	166.1	6.5	4.28	3251.9	1.5	4366	26.3
				Bb-2				
No U added	1	390.7	8.0	7.13	0.0	0.0	4398	11.3
	5	408.8	8.0	7.19	2783.7	1.2	4321	10.6
	11	379.1	8.0	6.66	5722.5	2.6	4250	11.2
	17	299.3	8.0	6.47	8247.5	3.7	4200	14.0
	26	284.0	8.0	6.86	10184.9	4.6	4152	14.6
	32	256.2	8.0	6.44	12133.9	5.4	4107	16.0
	38	222.0	8.0	5.95	13784.0	6.2	4071	18.3
	42	225.5	8.0	6.06	15103.7	6.8	4035	17.9
	47	208.1	8.0	6.78	16470.4	7.4	4003	19.2
	53	208.9	8.0	6.91	17880.3	8.0	3965	19.0
	59	191.6	8.0	6.71	19323.4	8.6	3931	20.5

Table 3, Continued.

	Cum. Days Elapsed	U conc., µg/L	Volume, mL	Aliquot kept, mL	Cum. U removed[1], ng	Cum. U removed[1], %	(U on solid - bkg), ng/g	K_d[2]
				C-1				
80 µg/L U added	11	420.3	8.0	0.500	0.0	0.0	4408.3	10.5
	21	354.9	7.5	6.509	210.2	0.1	4421.3	12.5
30 µg/L U added	32	298.2	8.0	0.500	2520.2	1.1	4373.3	14.7
	42	282.9	7.5	6.146	2669.3	1.2	4376.3	15.5
20 µg/L U added	53	276.8	8.0	0.500	4408.2	2.0	4331.8	15.7
	63	274.8	7.5	6.142	4546.6	2.0	4332.2	15.8
				C-2				
80 µg/L U added	11	440.7	8.0	0.50	0.0	0.0	4404	10.0
	21	370.5	7.5	6.47	220.4	0.1	4418	11.9
30 µg/L U added	32	348.8	8.0	0.50	2617.8	1.2	4360	12.5
	42	296.9	7.5	6.16	2792.2	1.2	4370	14.7
20 µg/L U added	53	278.4	8.0	0.50	4620.2	2.1	4326	15.5
	63	273.1	7.5	6.13	4759.4	2.1	4327	15.8
				Cb-1				
No U added	11	441.1	8.0	0.5	0.0	0.0	4387	9.9
	21	367.2	7.5	6.2	220.5	0.1	4402	12.0
	32	336.7	8.0	0.5	2510.1	1.1	4343	12.9
	42	269.5	7.5	6.1	2678.4	1.2	4356	16.2
	53	250.6	8.0	0.5	4315.8	1.9	4314	17.2
	63	203.1	7.5	6.2	4441.1	2.0	4323	21.3
				Cb-2				
No U added	11	431.8	8.0	7.160	0.0	0.0	4389	10.2
	21	357.8	8.0	6.682	3091.3	1.4	4323	12.1
	32	325.7	8.0	7.002	5481.9	2.5	4267	13.1
	42	268.7	8.0	6.100	7762.2	3.5	4219	15.7
	53	226.4	8.0	6.748	9401.4	4.2	4185	18.5
	63	194.8	8.0	6.977	10928.9	4.9	4151	21.3

[1]This refers to the uranium removed in all *previous* steps.
[2]Calculated using the background-subtracted concentration of U on the solid.

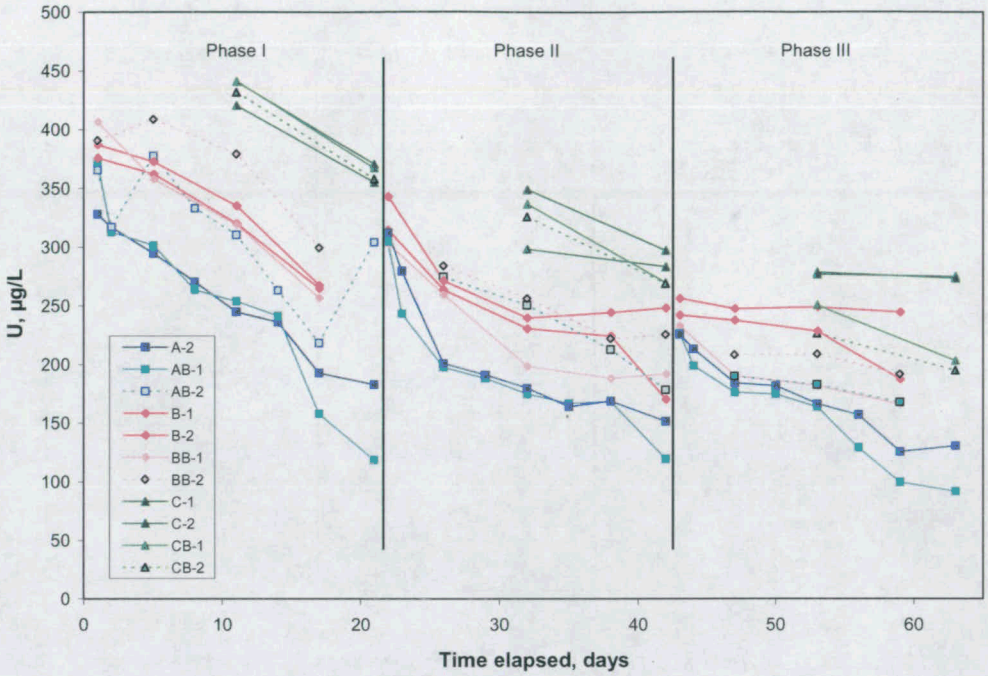

Figure 1. Concentration of uranium in sorption/desorption experiments. See Table 2 for a description of the sample sets listed in the legend.

sample at each sampling interval. Although 0.5 mL of the sample was retained, the remaining liquid, now degassed, was added back to the sample. Each of these effects is visible in trends of the reinfused, spiked samples. The concentration in the sample dropped rapidly with each 0.5 mL sampling, and then rebounded when fresh groundwater was added for the next phase. However, concentration did not rebound quite to the initial value, because the fresh groundwater had degassed slowly on the table-top.

This interpretation is consistent with the observed trends in uranium concentration, and is confirmed by the measured calcium data. As the water degassed, the pH rose, and calcium carbonate precipitated, resulting in a drop in the calcium concentration (Figure 2).

The different processes affecting the systems are clearer if subsets of the samples are examined. Figure 3 shows the results for the re-infused samples. These samples show the effects of degassing during centrifugation and sampling—the concentrations drop steeply in each phase, and, in general, drop more steeply for the systems that were sampled more frequently. They also rebound when fresh groundwater is added at the beginning of each subsequent phase. Now examine the first samples collected in the each phase. These samples had not been previously centrifuged, so show only the effects of degassing of the groundwater as it was stored on the tabletop, prior to being added to the samples. The initial uranium concentrations for phase one of the experiments, collected after one day of equilibration for the A and B sample sets, have the highest U values (from 328 to 407 µg/L). The first samplings for Phase II and Phase III are progressively lower. This indicates that the groundwater did degas as it was stored on the tabletop, over the 21-day extent of each phase. Note, however, that the C samples, collected after 11 days of equilibration, are consistently higher in U (420-441 µg/L) than the A and B samples for

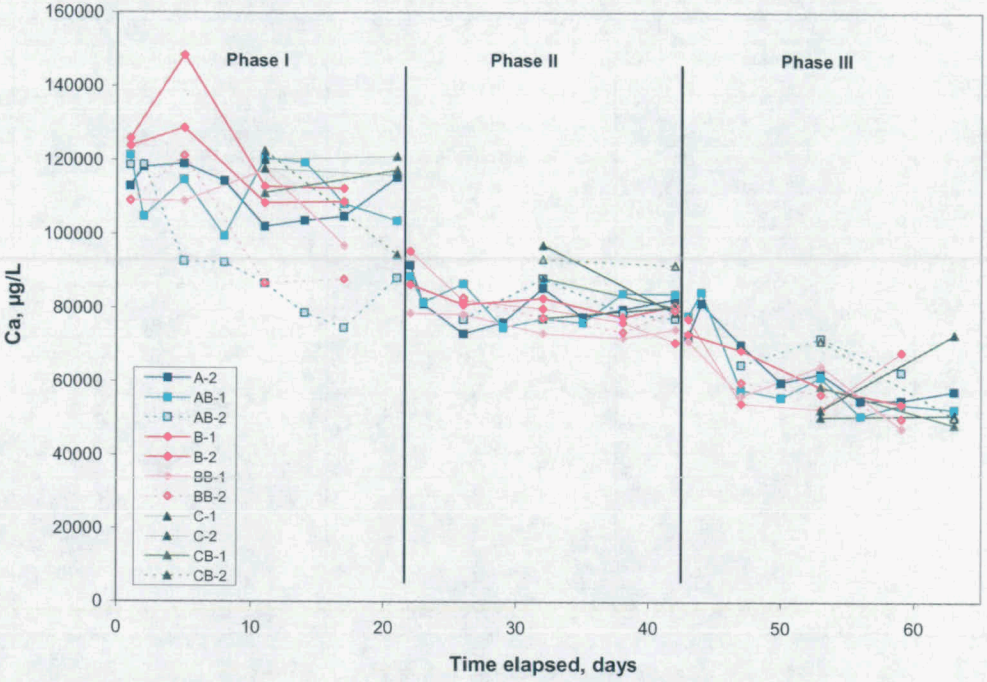

Figure 2. Concentration of calcium in sorption/desorption experiments. See Table 2 for a description of the sample sets listed in the legend.

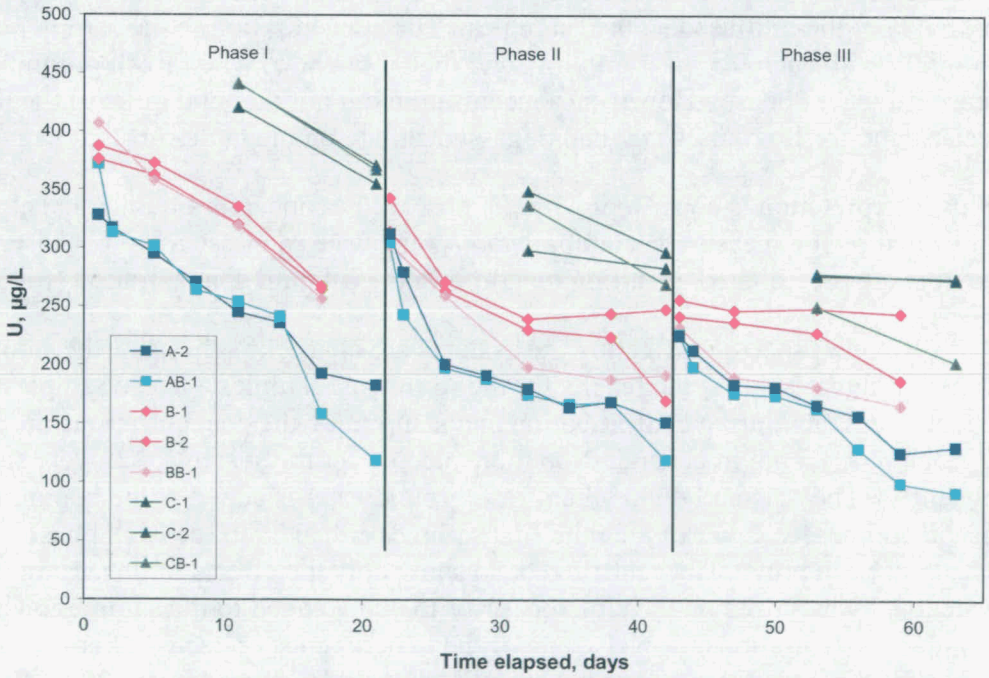

Figure 3. Concentration of uranium in systems which were sampled and re-infused.

each phase. This suggests that, within each phase, in the absence of degassing, U concentrations in solution would increase over time, as uranium continues to desorb slowly from the sediment. This is what is typically observed in sorption/desorption experiments.

The effect of degassing during centrifugation and sampling is clear—the samples that were sampled most frequently show the most rapid drop in U concentration (Figure 1), even though little U has been removed from the system. The full extraction samples also show a decrease in concentration, although they were not centrifuged and re-infused. This reflects both degassing of the groundwater on the tabletop and removal of uranium from the systems—in the most frequently sampled system (Ab-2), over 10% of the total uranium was removed from the system.

Because of the degassing, it is very difficult to quantitatively determine the labile and non-labile fractions of uranium in the samples. However, semi-quantitative arguments can be made. Initial K_ds, prior to significant degassing, cluster around 11–14 mL/g, after subtracting off the background uranium, (1.4 µg/g, as determined by Phase I of this study). This is a maximum K_d, as a significant amount of the uranium may be sequestered and not available for desorption.

Although the final liquid concentrations do not vary greatly between the different sets of samples, despite the fact that differing amounts of uranium—from 1 % to 11 %—were removed over the course of the sampling, there is a consistent difference in concentrations in the total extraction samples. Sample Ab (from which the most uranium was removed) consistently has lower U concentrations in solution than sample Bb, which in turn has lower concentrations than Cb, from which the least U was extracted (Figure 4).

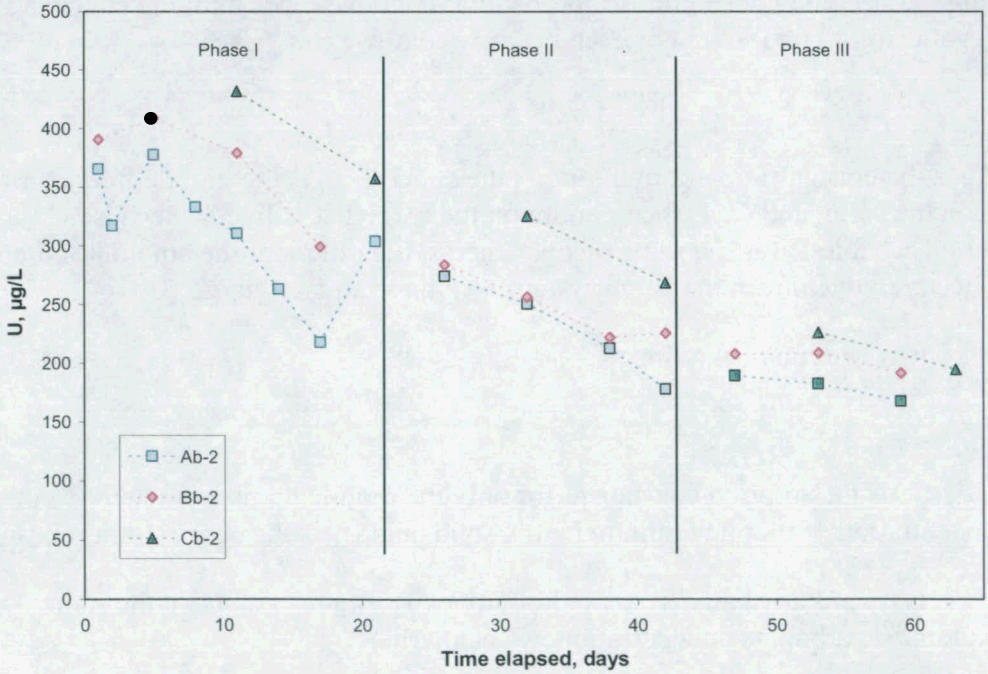

Figure 4. Concentration of uranium in total extraction samples. See Table 2 for a description of the sample sets listed in the legend.

Ideally, this difference could be used to determine the amount of non-labile or fixed U in each sample, as described below.

The total extraction samples were infused with fresh groundwater at each step, and concentrations began to level out at later sample times, those over 30 days. For these samples, degassing only occurred on the table top, not in the sealed sample containers (the groundwater in these samples was not centrifuged out and reinfused), so the carbonate content of the groundwater in samples prepared and collected at the same time should be similar. Under these conditions, the same K_d should apply to the samples, and differences in the uranium concentration in solution will be a function of two parameters:

1) the equilibration time for that step (e.g. sorption kinetics). Samples were equilibrated for intervals of 2 to 11 days before sampling. If desorption kinetics are slow, then the longer-equilibrated samples would be expected to have higher concentrations.

2) the amount of labile uranium remaining in the system. This varies because the batch systems have been sampled a different number of times. Sample Ab-2 was sampled a total of 15 times, removing 10.8% of the total U; sample Bb-2, 11 times, removing 8.6%; and sample Cb-2, 6 times, removing 4.9%.

The role of sorption kinetics can be minimized by considering samples collected after the same time interval. The effect of differing amounts of uranium remaining can be maximized by considering the total extraction systems, and samples collected late in the experiment, when significant amounts of uranium have been extracted from the samples. Thus, the concentration in solution should mostly be a function of the amount of labile uranium in the system (this assumes that there is a surplus of whatever sorption site is controlling the solution concentration--probably true at these low uranium concentrations and high solid:solution ratios). For each batch system, we can write:

$$C_S = C_{S(m)} + C_F \qquad \text{Eq. (1)}$$

Where C_S is the concentration of uranium on the solid, $C_{S(m)}$ is the mobile fraction of uranium on the solid, and C_F is the uranium on the solid that is fixed. Because C_F is fixed—not leachable—it is the same on all samples, regardless of the amount of uranium that has been removed from the batch system. All have units of ng/g.

For each system, we can also write:

$$K_{d(mobile)} = C_{S(m)}/C_L \qquad \text{Eq. (2)}$$

where $K_{d(mobile)}$ is the sorption coefficient for only the mobile uranium in the system, $C_{S(m)}$ is the concentration of mobile uranium on the solid, and C_L is the concentration in solution.

This is true of any batch system. For any two systems, that have the same groundwater and carbonate concentration, we can write:

$$K_{d(mobile)} = C_{S(m)a}/C_{La} = C_{S(m)b}/C_{Lb} \qquad \text{Eq. (3)}$$

And:

$$C_{Sa} = C_{S(m)a} + C_F \qquad \text{Eq. (4)}$$

$$C_{Sb} = C_{S(m)b} + C_F \qquad \text{Eq. (5)}$$

Solving for the $C_{S(m)}$ terms in equations (4) and (5) and substituting into equation (3) yields

$$\frac{(C_{Sa} - C_F)}{C_{La}} = \frac{(C_{Sb} - C_F)}{C_{Lb}} \qquad \text{Eq. (6)}$$

This can be solved for the fixed fraction on the solid:

$$C_F = \frac{C_{Sb}C_{La} - C_{Sa}C_{Lb}}{C_{La} - C_{Lb}} \qquad \text{Eq. (7)}$$

Thus, any pair of samples (Ab-2–Bb-2) can be used to calculate the amount of non-mobile uranium on the solid. This is best applied to those samples collected late in the experiment, as this is where the difference in the total uranium in the systems is greatest, where the groundwater can be expected to have degassed to a constant carbonate concentration, and where the effect of sorption kinetics can be expected to be least, since the sampling intervals are the same.

Table 4 shows the results for Ab-2–Bb-2 pairs of total extraction samples that were collected more than 40 days after the start of the experiment. The predicted amounts of U that is non-mobile are somewhat scattered initially, but cluster with increasing time; the last four data points average 4349 ng/g (this value, of course, includes the background U), or, after subtracting off the background U, 65.0% of the contaminant U appears to be fixed.

The C_F values calculated for the Ab-2–Bb-2 sample pairs in Table 4, presumably most reliable because these were sampled at equal sample intervals, can be used with the initial measured K_ds in each sample set calculate $K_{d(m)}$. The initial values for each sample set are used, because we are interested in the $K_{d(m)}$ that is applicable to the un-degassed groundwater. The average C_F for the last 4 values is 4349 ng/g. Using this value results in the $K_{d(m)}$ values for the A and B sets (sampled after one day) of 3.6 to 4.5 mL/g. The C sets (sampled for the first time after 11 days) yield values from 3.3 to 3.5 mL/g, reflecting the continued slow desorption of uranium.

The K_d calculated for the C set seems most relevant, because of the longer

Table 4. Calculated amount of U that is nonlabile.

day	C_L		C_S		C_F	
sampled	A	B	A	B	ng/g	%*
42	178.2	225.5	5300	5435	4791	75.1
47	189.8	208.1	5271	5403	3902	54.8
53	182.7	208.9	5238	5365	4352	65.1
59	167.8	191.6	5209	5331	4349	65.0

* of contaminant U, after subtracting out background

equilibration time. However, it is unlikely that equilibrium with respect to sorption-desorption has been reached even in the C case. To evaluate this, the kinetics of uranyl desorption were examined. The first samplings of the blank sample sets Ab-2, Bb-2, and Cb-2 were used to evaluate this. These samples were prepared using the initial, un-degassed groundwater, and sampled at either 1 day (Ab-2 and Bb-2 samples) or 11 days (Cb-2 samples). The second set of samples collected from Ab-2 and Bb-2 were also used, as it is unlikely that any significant degassing had occurred between the first and second days. These were re-infused with fresh groundwater on day 2, and resampled after an additional one and four days, respectively.

All of these samples are plotted in Figure 5, and a clear trend of increasing concentration with equilibration time can be seen. A best-fit line of logarithmic form has been placed through the points. Theoretically, this trend should level out to a steady-state value after a long enough time interval. Because of the paucity of data points and the scatter in the data, this does not occur, although the rate of growth does level out considerably. Thus, the predicted K_d is dependent upon the water-rock contact time. This is illustrated in Figure 6, where K_ds predicted using the best fit line in Figure 5 are plotted as a function of time. Two cases are shown. The first calculates the K_d assuming that all uranium present above the background concentration is labile. The second uses the results of the analysis discussed above, and assumes that 4349 ng/g U is fixed. These two cases bound the likely range of conditions present in the sediment. As the Fernald aquifer remediation project is currently pumping 3 pore volumes of water through the aquifer each year, a contact time that is relevant to the project is 1/3 year, or 122 days. This corresponds to predicted K_ds of 8.7 mL/g and 2.8 mL/g, if the contaminant U is assumed to be completely labile or mostly fixed, respectively.

We can use these values to bound the number of pore volumes necessary for pump-and-treat remediation to reduce the groundwater concentrations to less than the EPA limit of 30 ng/mL. This is shown in Figure 7. Assuming that all contaminant U is labile, and that a K_d of 8.7 mL/g is appropriate, 123 pore volumes are necessary to reduce the U contamination in the groundwater to less than 30 ng/mL. If 65% of the contaminant U is assumed fixed, and a $K_{d(mobile)}$ of 2.8 mL/g is assumed for the remaining mobile material, then about 41 pore volumes are required (note that, in this case, the fixed fraction constitutes a progressively larger portion of the uranium remaining on the solid, so the actual K_d increases from 8.7 mL/g initially, to ~106 mL/g when the groundwater concentration drops below 30 mL/g). By the end of 2003, about 21.3 pore volumes had been pumped at the Fernald site.

However, these numbers assume that all of the sediment is in contact with all of the groundwater, at all times. At the site, the aquifer water level fluctuates seasonally and with rainfall, and fresh uranium is flushed out of the overlying sediments every time the water level rises. Because pumping mediates the water level rise, it probably slows the depletion of the uranium reservoir represented by the contaminated sediments above the water table. It might be useful turn off the pumps periodically, allowing the water table to rise on a regular basis and flush the overlying sediments. This would have the added benefit of allowing longer desorption time, resulting in a slightly higher release from the sediments below the water table.

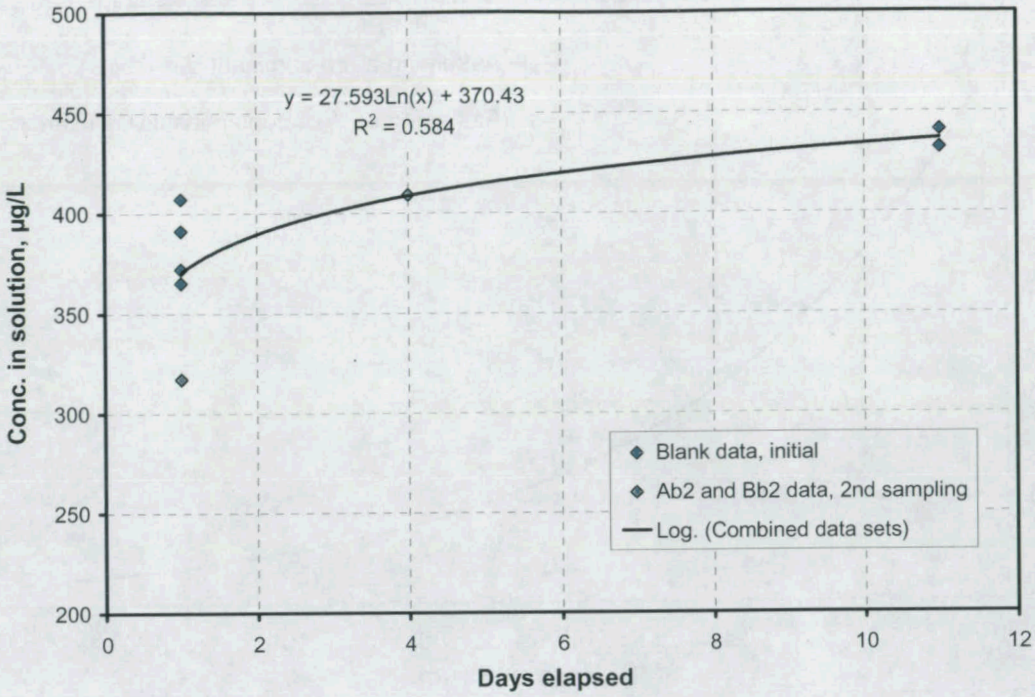

Figure 5. Kinetics of Uranium Desorption from Great Miami Aquifer Sediments.

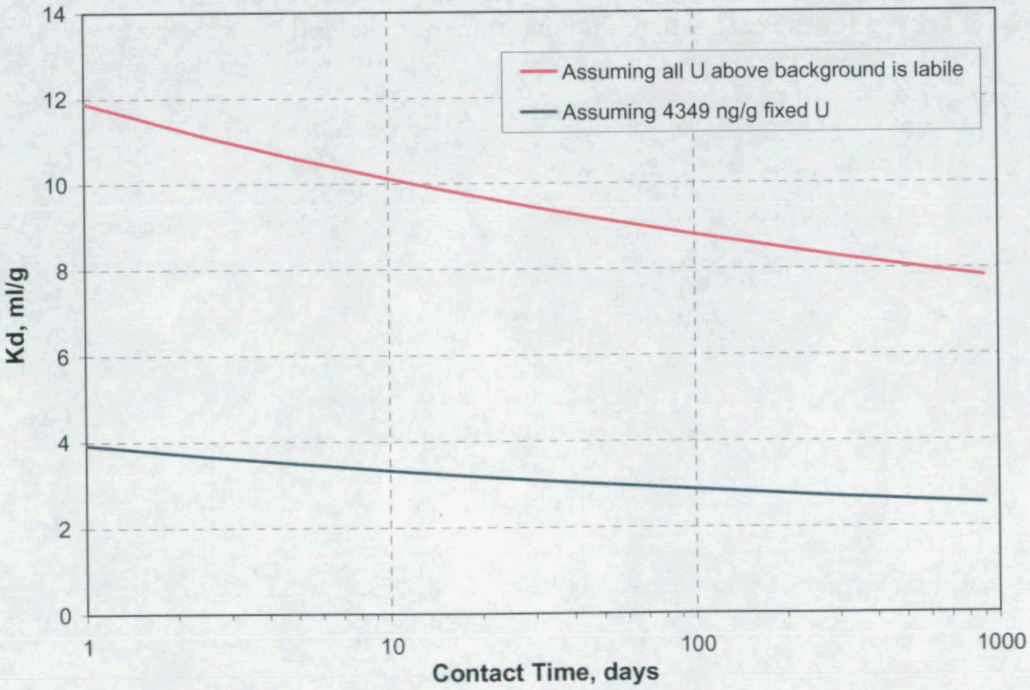

Figure 6. Predicted change in K_d with equilibration time.

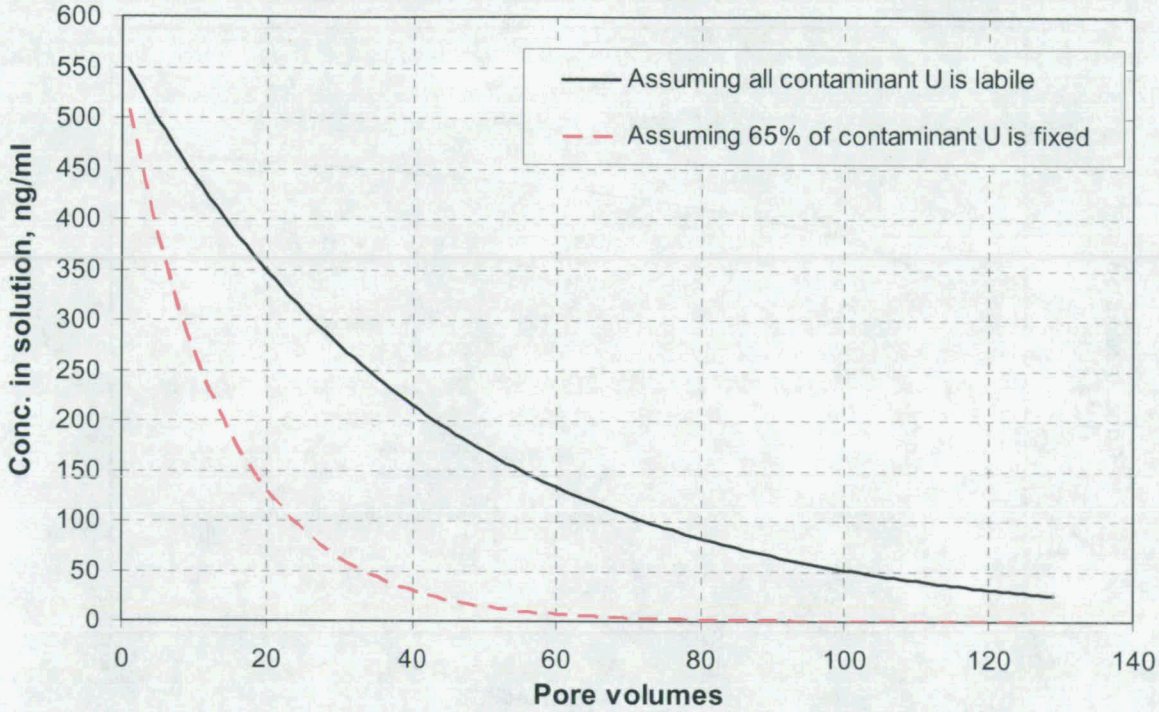

Figure 7. Predicted change in groundwater concentration with pore volumes treated. Assuming a $K_{d(mobile)}$ of 2.8 mL/g for the case where 65% of the contaminant U is fixed, and a K_d of 8.7 mL/g for the case where all contaminant U is labile.

5434

4.2 Results of Microanalytical Characterization

Several microanalytical techniques were used to evaluate the distribution of uranium in the sediments. These include electron microprobe and scanning electron microscope (SEM) analysis; secondary ion mass spectrometry (SIMS); and high-resolution transmission electron microscope (HR-TEM) analysis. Detailed descriptions of these techniques, including sample preparation, instrument calibration, and analytical conditions, are presented below.

4.2.1 Electron Microprobe Analyses

Element Mapping and Chemical Analysis

KD33262. X-ray mapping for U was done initially to search for areas of U concentrations and thus to locate potential targets for more detailed SIMS analysis. Sample KD33262 52.75'-53.75' had the highest uranium concentration (5.9 µg/g U) measured in a wood-free sediment sample in Phase I of this study. One map was done on the polished section of this sample. The map (Figure 8) covered 25.5 by 2.5 mm at 2.5 µm steps, requiring 30 hours to complete. From the results of that map, there appeared to be a slight correlation between U and Al when the elemental values of the map pixels were plotted (Figure 9), meaning that U may be associated with clays. Two new polished sections (KD33262A and KD33262B) were made from the raw sample since the original polished mount would not fit in the SIMS. Ion microprobe analyses (discussed below) were done on several targets, including clays and carbonate grains, on the new polished sections. One of the target areas is illustrated in Figure 10. An electron microprobe map was done on this area in KD33262A after it had shown positive results for U in the SIMS. The element map (Figure 11) attempted to precisely locate the U in a pocket of detrital clay and other minerals attached to a calcite grain. The bright areas in the BSE image in Figure 10 are probably residual gold left behind from the gold coat that was applied for SIMS analysis and remained despite heavy polishing of the surface prior to application of the carbon coat for microprobe analysis. The uncorrected uranium map mirrors the bright areas, but they do not appear in the background subtracted U-map at the bottom of Figure 11. Based on the corrected U-map, it is apparent that the attempt to find the uranium in the sediment was unsuccessful using the electron microprobe.

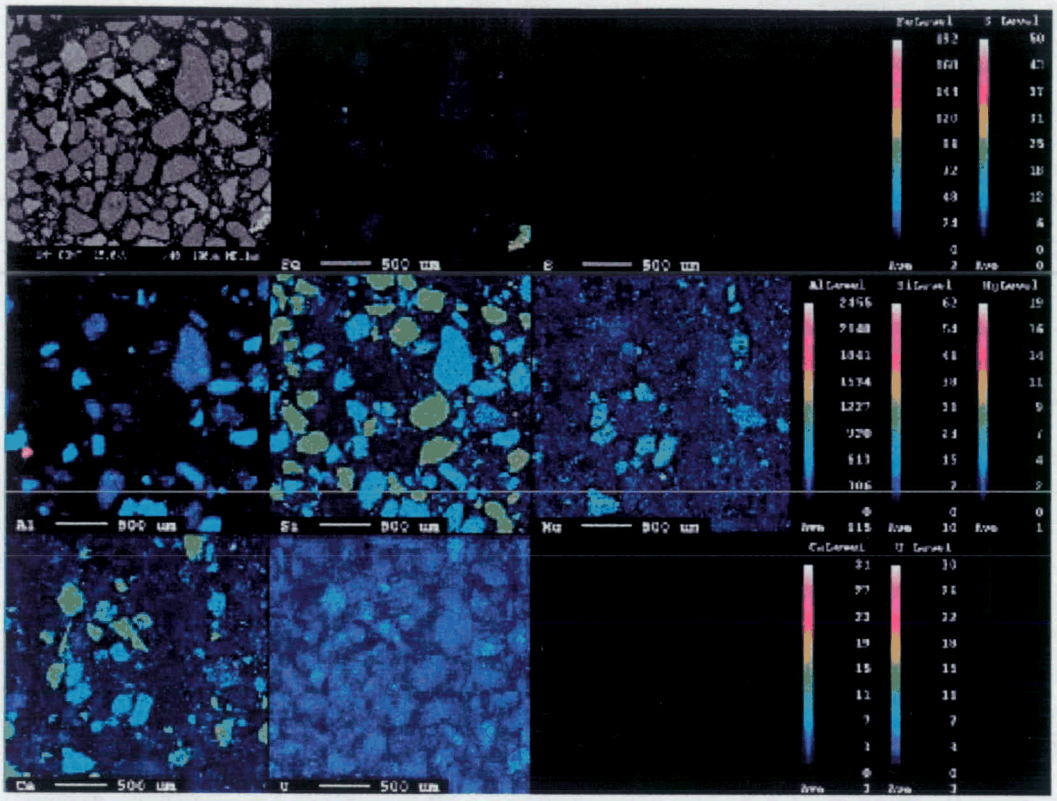

Figure 8. KD33262 52.75'–53.75'. BSE image of an area near the center of the polished section. Scale bars are 500 µm.

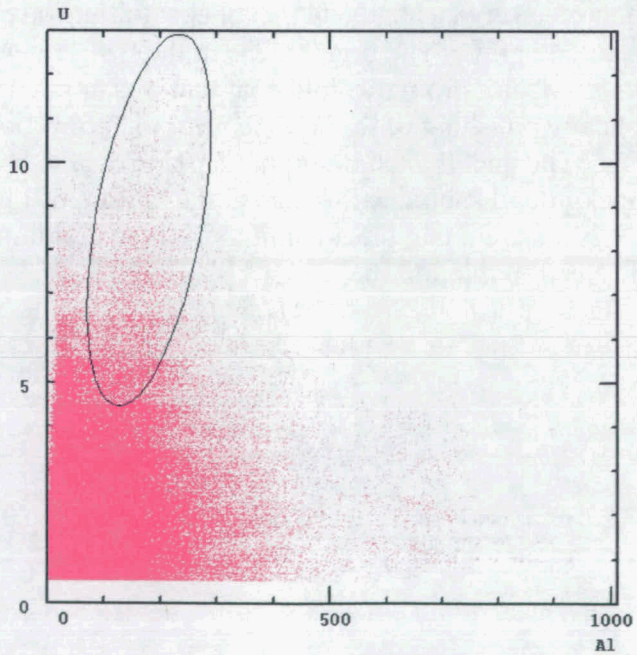

Figure 9. Plot of Al x-ray intensity vs. U intensity from each pixel of map on KD33262 52.75'–53.75' (Figure 8). Circled area indicates a possible correlation between U and Al.

5634

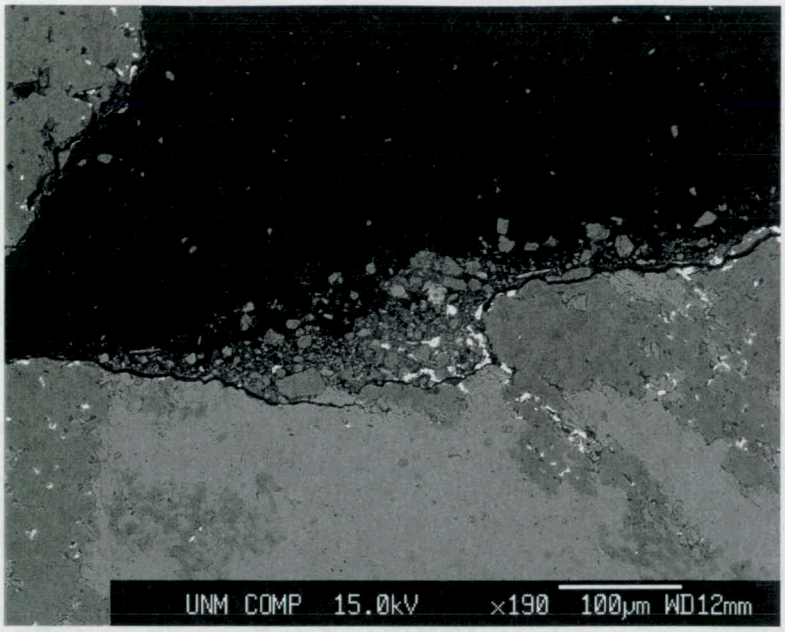

Figure 10. KD33262A. A pocket of detrital minerals on the side of a quartz and calcite pebble, one of the areas targeted for SIMS analysis. Material in the pocket was analyzed by SIMS and electron microprobe. See Figure 11 for details.

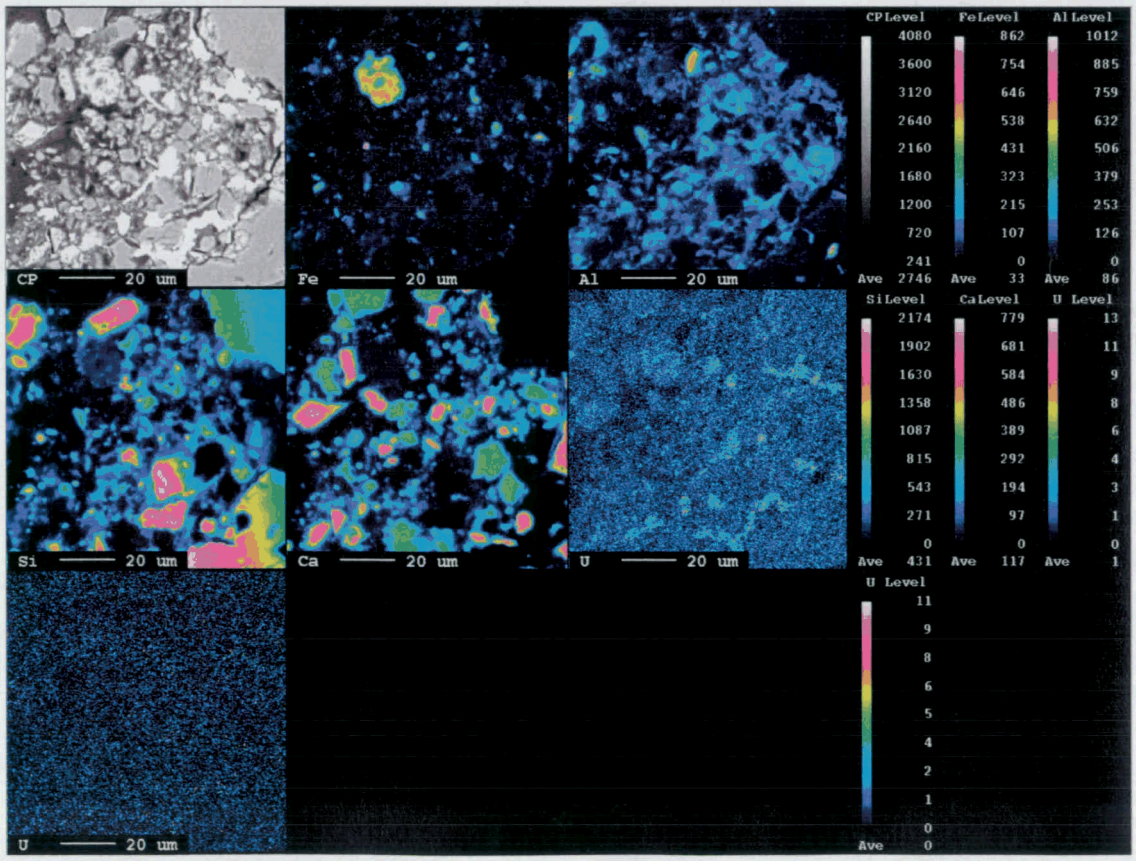

Figure 11. KD33262A. Element maps from the detritus pocket in Figure 10. The bright areas in the BSE image (upper right) are probably residual from the SIMS gold coat. The lower U-map has been background subtracted.

KD33298. The sample KD33298 had the highest values of U as measured by Sandia Laboratories and consisted of fragments of charcoal or small diameter carbonized tree limbs. The carbonized wood contained scattered pyrite and soil. Three maps were produced on a polished sample. The area of each map included pyrite, detrital clay and sand, and some of the wood in one of the maps. The pyrite consisted of multiple framboidal bodies, often attached in a chain-like fashion. The individual round framboids are usually less than 20 μm in diameter. The area of the first map is shown in the backscattered electron (BSE) image in Figure 12a, and the element maps are displayed in Figure 12b. In these maps, the high Al areas are clays, which will also have high Si levels. The highest Si concentrations are quartz. The high Fe portions will be pyrite, since there is apparently little oxidized Fe present in this sample. The lower three maps in Figure 12b contain information for U: the left image is the raw count data; the middle image contains the background counts for U, in this case collected at the indium spectral position and thus labeled; and the right image is the raw counts with the background counts subtracted. The effect of higher average atomic number, as in the pyrite, can be seen in the raw U image. A phase with a higher average atomic number will have a higher background and will result in an "apparent concentration" of any trace element that is mapped. Thus it appears that U is concentrated in the pyrite simply by virtue of its higher atomic number and higher background counts compared to the surrounding silicate materials. For this reason the background counts must be subtracted before trace levels of U can be evaluated. The residual uranium count rate indicates that U is present in this cluster of pyrite; the concentration level will be discussed below.

Elemental maps were collected on two additional clusters of pyrite in other areas of the sample. The second map (Figure 13a) was collected on an area with both solid framboidal pyrite groups and clusters of loosely packed pyrite octahedrons; the maps are shown in Figure 13b. The framboids are located almost entirely within carbonized wood. The final map on this section is illustrated in Figure 14a and the element maps in Figure 14b. The framboids at this location are contained within detrital silicates at the edge of a wood fragment. The third map is a "free shape" map that allows the operator to define unusual shapes in order to avoid undesirable areas such as epoxy that will degrade under the electron beam. Unfortunately, this type of map does not permit manipulations such as background subtraction, and therefore the uranium map in Figure 14b is not background subtracted.

5634

Figure 12a. KD33298. BSE image of framboidal pyrite (white) surrounded by clay and detrital grains of calcite, dolomite, quartz, and feldspar (medium gray). Dark gray represents epoxy-filled voids. Scale bar is 10 μm. Numbers refer to electron microprobe analyses in Table 6.

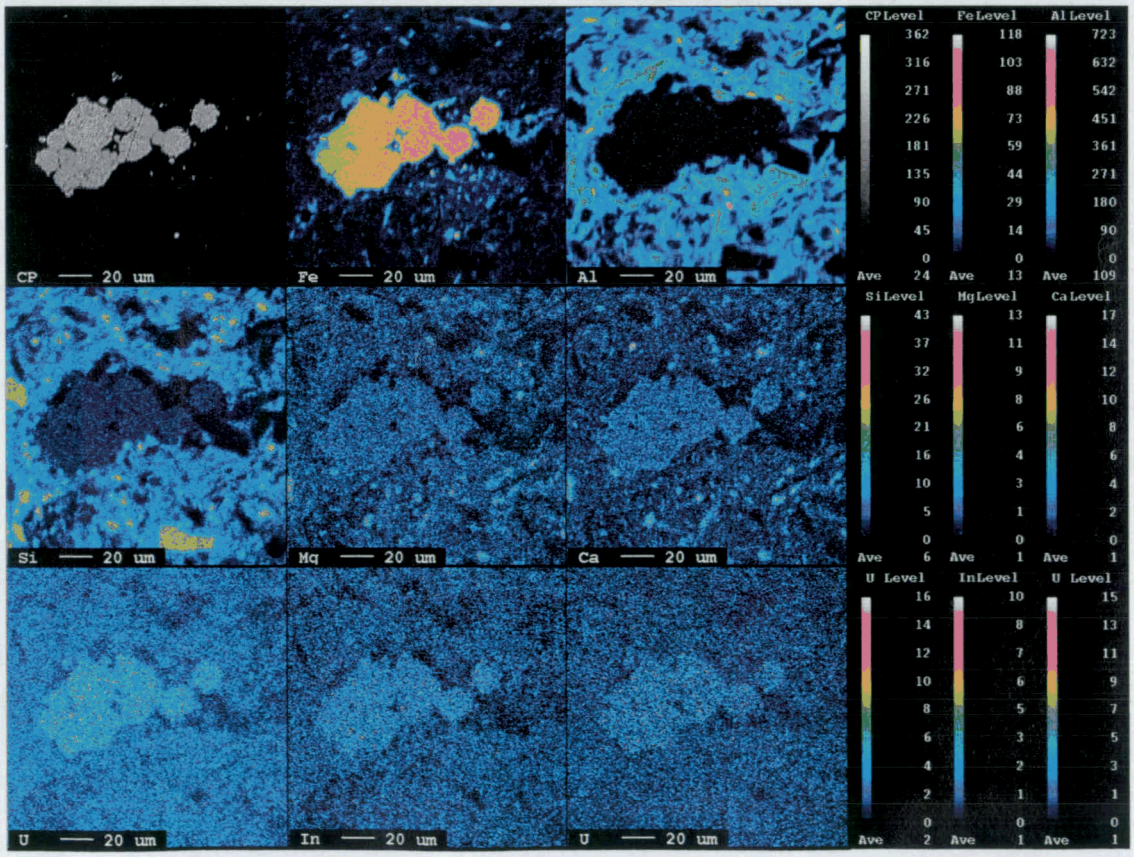

Figure 12b. KD33298. Element maps collected over area shown in Figure 12a. Brighter or "hotter" colors represent higher concentrations. Intensity scales at right are in x-ray counts.

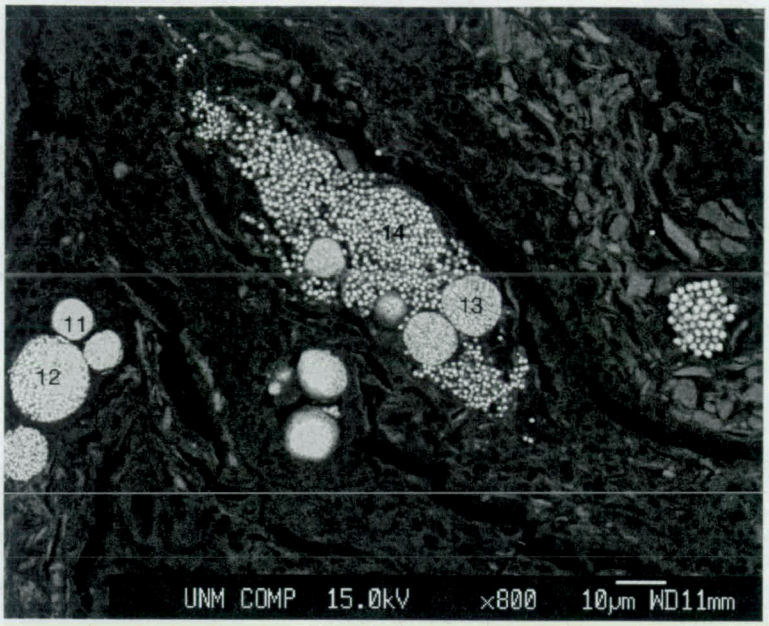

Figure 13a. KD33298. BSE image of framboidal pyrite (white) and clusters of loose pyrite octahedral within charcoal (dark gray). Scale bar is 10 µm. Numbers refer to electron microprobe analyses in Table 6.

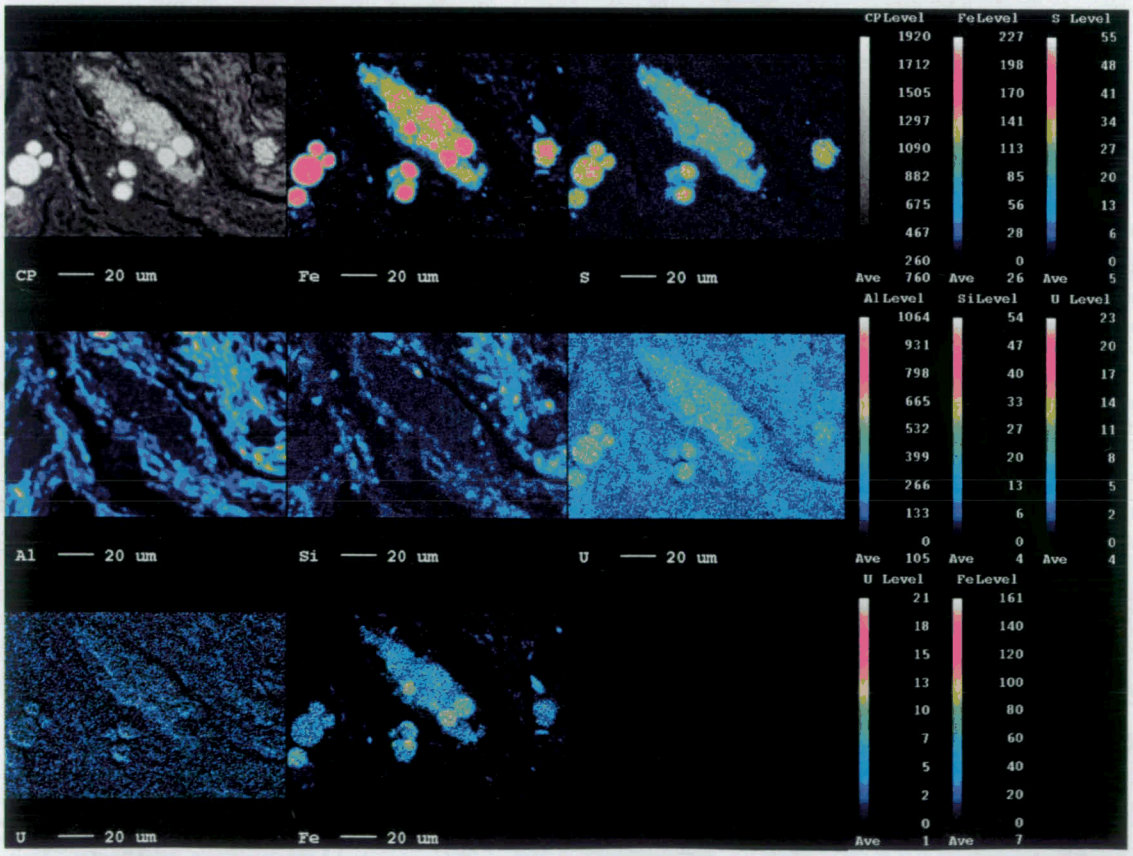

Figure 13b. KD33298. Element maps collected over the area in Figure 13a. The lower U-map has the background subtracted. The lower Fe map is a result of subtracting the S-map from the Fe-map. The brighter objects in that image have lower sulfur relative to pyrite.

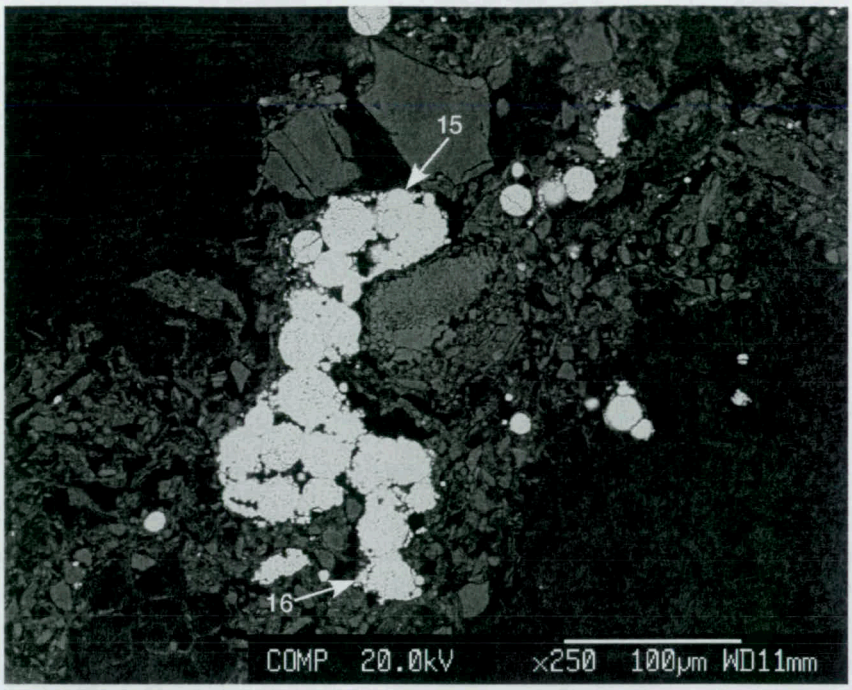

Figure 14a. KD33298. BSE image of framboidal pyrite (white) in detrital silicates (medium gray). Pitted, dark gray material is epoxy. Scale bar is 100 µm. Numbers refer to electron microprobe analyses in Table 6.

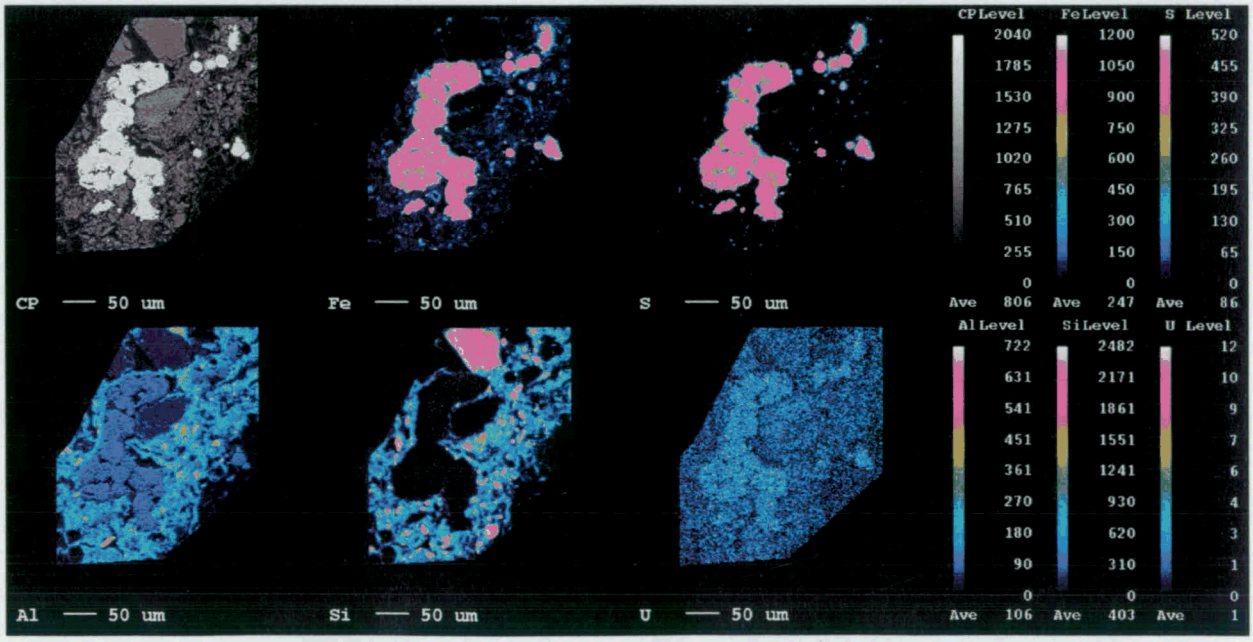

Figure 14b. KD33298. Element maps collected over part of the area in Figure 14a.

Electron Microprobe Chemical Analyses

Following element mapping, quantitative x-ray microanalysis was done on some of the map targets to supplement the ion microprobe analyses. For example, SIMS analyses were not performed on the pyrite mapped in KD33298, so these were analyzed with the assumption that the uranium concentration would be higher and therefore detectable by electron microprobe. Analysis of detrital materials was done on both KD33298 and KD33262; results were shown in Table 5. The analytical totals are low due to the small particle size and porous nature of the silicate/carbonate detritus. Most of the analyses probably represent mixed phases, although dolomite is clearly present in analyses #4 and 7. These were the only analyses with detectable uranium. Note that these analyses are at or just below the 2σ detection limit.

Results from KD33298 pyrite analyses are found in Table 6. The samples typically exhibit low analytical totals due to the porous nature of the pyrite and the small particle size of the pyrite octahedra. Most of the large framboids contained no measurable uranium. However, the element was detected in some of the smaller framboids, particularly those around the outside of larger clusters. Uranium was also detected in what appear to be overgrowths encrusting larger pyrite (e.g. Figure 14a, analyses 15 and 16). The large cluster of loose pyrite octahedral observed in Figure 13a also contained detectable uranium. This cluster exhibits lower sulfur than stoichiometeric pyrite (Figure 13b and Table 6, analyses 13 and 14); the formula for these two analyses would be Fe_2S_3, a pyrrhotite group mineral.

Table 5. Electron microprobe analyses of detrital material attached to pebbles in KD33262 or associated with pyrite in KD33298. Analyses 1-7 are on KD33262A, 8-12 are on KD33298.

No.	SiO_2	Al_2O_3	MgO	FeO	CaO	K_2O	UO_2	Total	Comment
1	13.48	5.42	5.74	3.97	17.08	0.75	BDL	46.44	Clay on qtz/cc Figure 11
2	15.67	5.64	9.65	2.80	15.95	0.91	BDL	50.62	Clay on qtz/cc Figure 11
3	15.64	8.92	4.04	5.36	14.81	1.33	BDL	50.10	Clay on qtz/cc Figure 11
4	1.61	1.42	18.01	0.68	27.41	0.22	0.009	49.37	Dol. on qtz grain no figure
5	27.89	9.68	3.24	2.56	13.24	2.35	BDL	58.96	Clay on qtz grain no figure
6	38.18	7.81	1.40	3.19	2.14	1.94	BDL	54.66	Clay on qtz grain no figure
7	2.32	1.62	17.55	0.96	26.34	0.36	0.008	49.15	Replicate analysis #4
8	49.53	26.61	1.48	1.96	1.04	6.48	BDL	87.09	Clay in Figure 14
9	30.47	13.87	7.27	4.32	9.97	3.08	BDL	68.97	Clay in Figure 14
10	17.24	9.48	9.84	2.07	13.13	2.43	BDL	54.20	Clay in Figure 12
11	49.14	13.11	1.95	2.80	1.99	5.11	BDL	74.09	Clay in Figure 12
12	39.94	18.03	2.98	5.36	1.57	4.20	BDL	72.08	Clay near area in Figure 12

Note: BDL = below 2σ detection limit (~0.0105 Wt% UO_2)

Table 6. Electron microprobe analyses on pyrite in sample KD33298.

No.	Fe	S	U	Total	Comment
Element %					
7	44.45	51.61	BDL	96.07	Figure 12, large framboid core
8	42.46	50.07	0.012	92.54	Figure 12, small framboid core
9	43.62	51.65	BDL	95.27	Figure 12, med framboid core
10	41.72	49.31	0.011	91.04	Figure 12, small framboid on rim
11	44.15	52.02	BDL	96.17	Figure 13, small framboid
12	44.19	50.99	BDL	95.19	Figure 13, large framboid
13	43.73	37.01	0.013	80.75	Figure 13, framboid with cluster
14	39.98	38.05	0.013	78.05	Figure 13, loose cluster
15	44.30	52.26	BDL	96.56	Figure 14, overgrowths on framboids
16	44.44	51.58	0.009	96.03	Figure 14, overgrowths on framboids
Average	43.30	48.46	0.009	91.77	
Atomic %					
7	33.083	66.916	BDL	100	Figure 12, large framboid core
8	32.740	67.258	0.002	100	Figure 12, small framboid core
9	32.650	67.349	BDL	100	Figure 12, med framboid core
10	32.688	67.310	0.002	100	Figure 12, small framboid on rim
11	32.756	67.242	BDL	100	Figure 13, small framboid
12	33.219	66.780	BDL	100	Figure 13, large framboid
13	40.417	59.580	0.003	100	Figure 13, framboid with cluster
14	37.625	62.372	0.003	100	Figure 13, loose cluster
15	32.730	67.270	BDL	100	Figure 14, overgrowths on framboids
16	33.090	66.909	0.002	100	Figure 14, overgrowths on framboids
Average	34.100	65.899	0.002	100	

Note: BDL = below 2σ detection limit (~0.0092 Wt% U)

4.2.2 Ion Microprobe Analyses

Element Mapping and microanalysis

Ion microprobe analyses were conducted on KD33262A and KD33262B. Based on the potential correlation between Al and U that was found by the electron microprobe, several pockets of detrital clay-sized materials attached to larger pebbles were targeted, along with clay "balls," or detrital shale pebbles (Figure 15 and 16). Calcite, dolomite, and quartz pebbles were also examined (Figure 17). In addition to the clay pockets, the host rock on which the pockets occurred was also analyzed to verify that the measured uranium values were in the attached clay and not the host rock. The results are provided in Table 7.

Most of the clays contained high uranium values, ranging from 23 µg/g to as much as 153 µg/g. The pockets of clays and detrital minerals adhering to larger pebbles had the highest uranium concentrations. For example, the pocket along the side of the pebble in

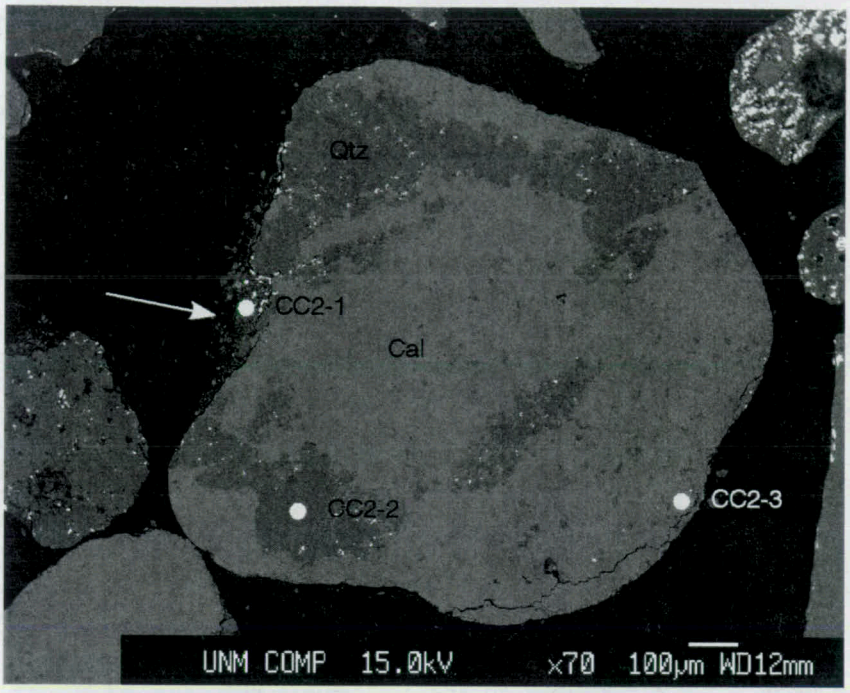

Figure 15. KD33262A. A quartz (Qtz) and calcite (Cal) sand grain. The arrow points to the pocket of detrital minerals shown in Figure 7. Numbers refer to SIMS analyses in Table 7, and white spots locate the approximate point of analysis.

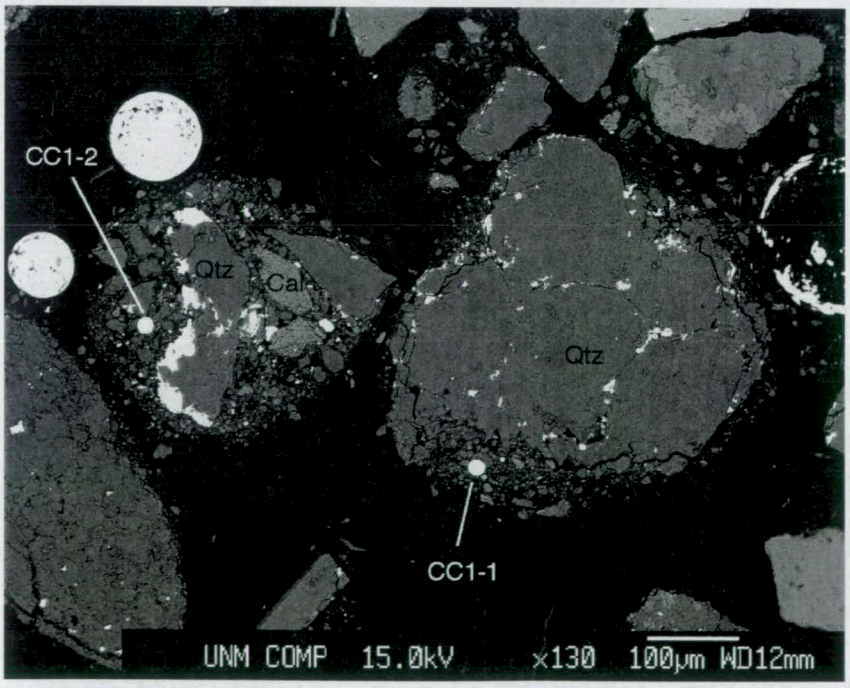

Figure 16. KD33262A. A "clay ball" at the left and on the right, a quartz pebble coated with detrital clay and other minerals. The bright areas are residual gold coat. Numbers refer to SIMS analyses in Table 7, and white spots locate the approximate point of analysis.

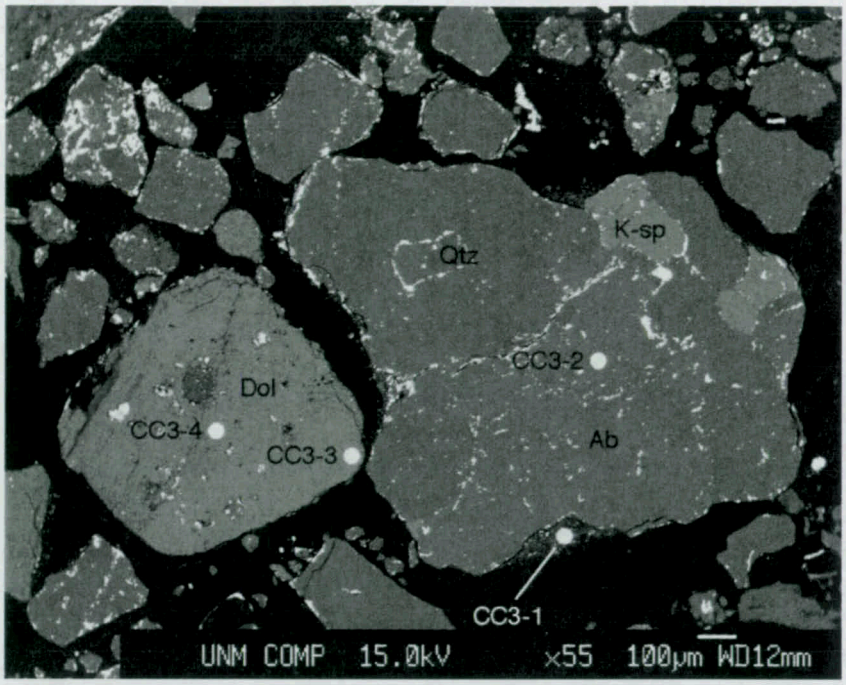

Figure 17. KD33262B. The composite pebble on the right consists of quartz (Qtz), potassium feldspar (K-sp), and albite (Ab). On the left is a dolomite pebble. Numbers refer to SIMS analyses in Table 7.

Table 7. Results of SIMS analysis for uranium in KD33262.

Sample	Intensity (counts)	Corrected Intensity	Concentration (μg/g)
Silicates			
CC1-1 (clay)	1.29817	0.64910	152.64
CC1-2 (clay)	0.19227	0.09610	22.61
CC2-1 (clay)	0.44761	0.22380	52.63
CC2-2 (quartz)	0.00372	0.00190	0.44
CC2-3 (calcite rim)	0.0342	0.0171	2.21
CC3-1 (clay)	0.51843	0.25920	60.96
CC3-2 (quartz)	0.00229	0.00110	0.27
CC3-3 (dolomite rim)	0.0212	0.0106	1.37
CC3-4 (dolomite core)	0.0272	0.0136	1.75
*C1-1 (clay)	0.63791	0.31900	75.01
*C1-2 (clay)	0.16670	0.08340	19.60
*C1-3 (calcite)	0.0107	0.0053	0.69

*No figure shown

Figure 15 contained 53 µg/g U (analysis CC2-1) while the host quartz and calcite that make up the bulk of the pebble contained very low concentrations, only to 2 µg/g. Several analyses were taken at the rims and cores of grains to look for higher concentration at the rim that may indicate adsorbed uranium (e.g. CC3-3 and CC3-4). However no differences were noted. This may be due to the large diameter of the SIMS beam relative to any thin layer of adsorbed uranium on the surface. A sorbed layer would probably be swamped by noise from the 5-10 µm ion beam.

Depth Profiling

Unwashed pebbles. To test whether a sorbed layer of uranium may be present on the surface of larger pebbles, four pebbles were mounted for ion depth profiling. The pebbles were designated pebble 1, a calcite fossil shell fragment; pebble 2, a smooth calcite pebble; pebble 3, a smooth quartz grain; and pebble 4, a smooth dolomite. The pebbles were taken as is, directly from the mixed gravel sample. Loose dust was blown off but the pebbles were not washed prior to mounting and gold coating. This left any adhering clays or detrital particles intact on the surface, which is illustrated in Figure 18. Surface clays and Fe-oxides can be seen in detail in Figure 19. Many of these small particles are authigenic and have grown on the surfaces of the pebbles, illustrated in Figure 20. Both the clays and Fe-oxides are potential getters for uranium.

The depth profile typically starts with a low-intensity signal and builds rapidly as the gold coat is eroded by the incoming primary ions, and secondary ion production increases. The SIMS rasters the ion beam over an area ~150 microns square, sequentially analyzing for each element of interest and then repeating the cycle. The ion signal tends to peak after a few cycles and will then begin to decline. If the element of interest is present only near the surface, then the decline in ion signal intensity tends to be rapid as the material is eroded away by the ion beam. However, if the element is present in the substrate, then signal decline tends to be much slower. The intensity tends to decline for all elements over time, even for the substrate elements, as implanted ions and charge build up at the surface. Figure 21 and 22 show the ion-etch pits after depth profiling. Because the surface has different types and amounts of material adhering to it, ion excavation is uneven: deep pits will be etched in some areas where ion removal is rapid while only small amounts of material will be removed where ionization is slower. This is demonstrated in Figure 22, which shows that the etched surface is extremely irregular. Thus it is difficult to estimate the true depth of the profiling.

The results of depth profiling on three pebbles are shown in Figures 23, 24 and 25. The fourth pebble (dolomite) was not done because of technical problems with mounting the ion probe grid. Pebble 1, the calcite fossil fragment, demonstrates a weak initial kick for Al and Si in both areas that were analyzed (Figure 23 A and B), due to clay on the surface. More clay is apparently present in the second analysis, based on the response of Al and Si (Fig 23B). Iron was analyzed in the second area and was apparently present on the surface, as indicated by the initial peak in the Fe plot in Figure 23B. Uranium shows a uniform slope in both plots at background levels.

5634

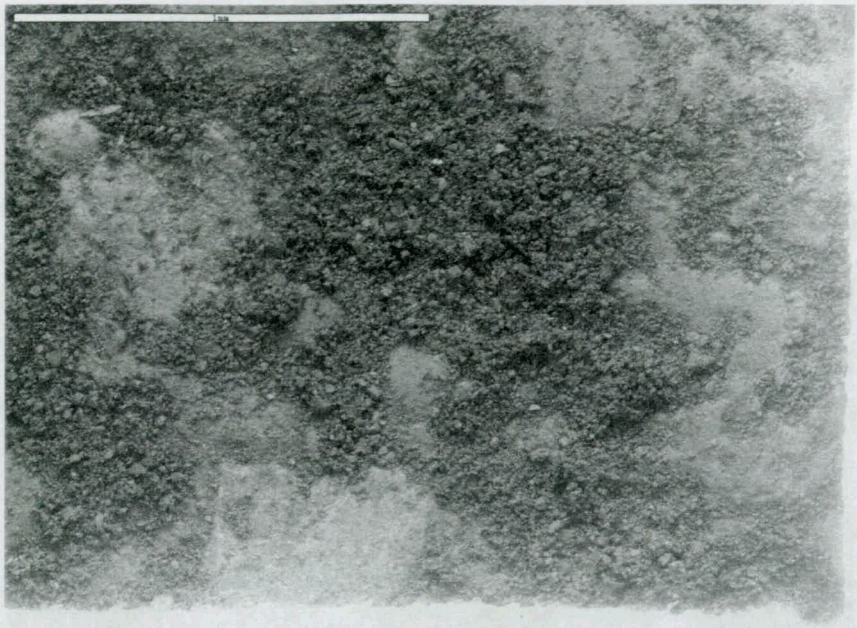

Figure 18. KD33262. BSE image of the gold-coated surface of pebble 1 (calcite). The smooth, light gray areas are the bare surface of the calcite pebble and the rough dark areas are adhering clay and detrital particles. Bright white bar along the bottom and right side is the tantalum SIMS grid that holds the pebble in place. Scale bar is 1 mm.

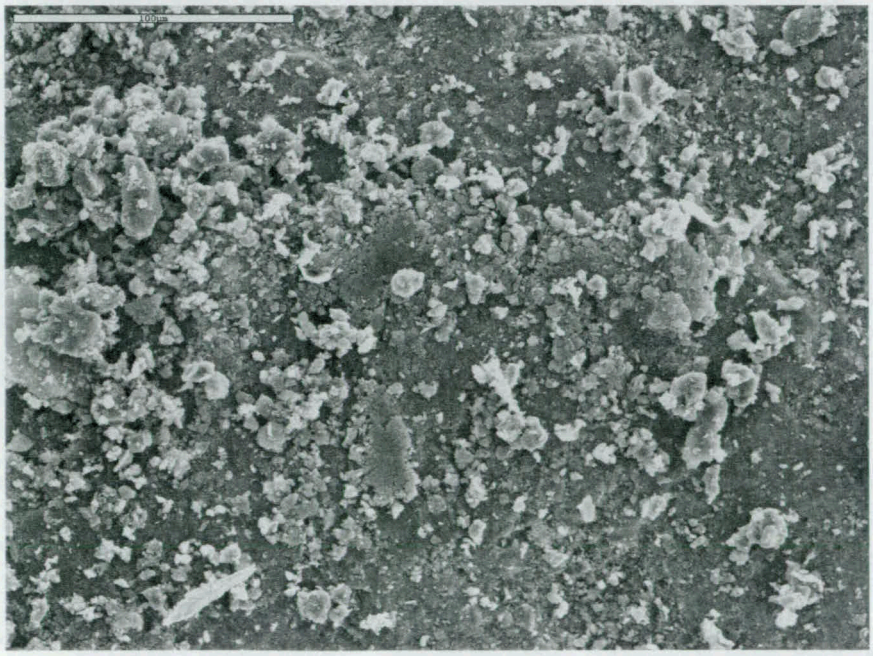

Figure 19. KD33262. SE image of the surface of pebble 2 (calcite). This image shows illite clays and iron-oxides that decorate the surface of the calcite pebble. Detrital feldspars, quartz and carbonates cling to the surface and to the clays. Depth profiling targeted the entire area of this image. Scale bar is 100 µm.

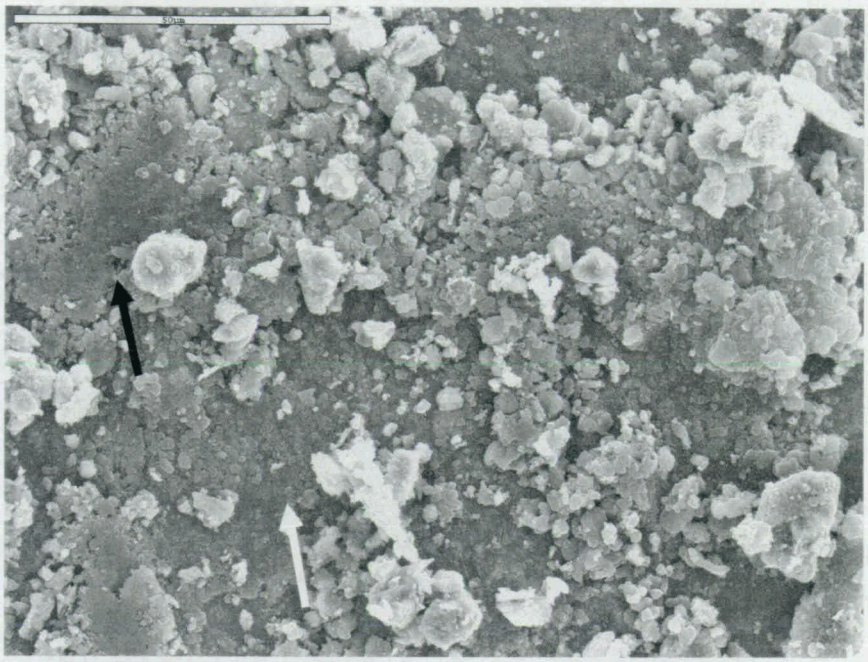

Figure 20. KD33262. Higher magnification SE image of authigenic minerals shown in Figure 19. Black arrow points to clay and white arrow points to Fe-oxide on the pebble surface. The larger irregular particles are detrital silt grains. Scale bar is 50 µm.

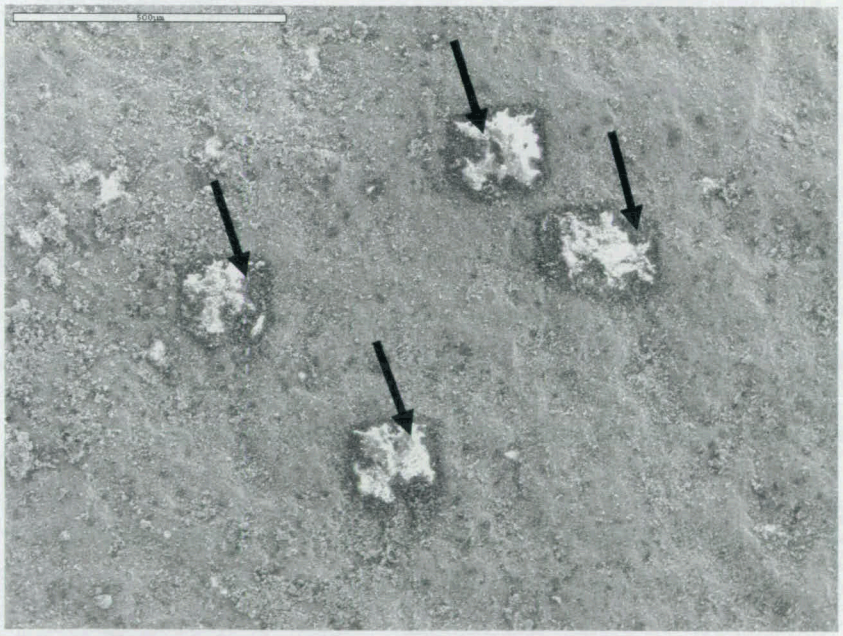

Figure 21. KD33262. SE image of the gold-coated surface of pebble 2 after SIMS depth profiling at four locations (arrows). The approximately square areas are the result of the ion beam raster that ionizes and removes the gold coat. The raster scars are charging under the electron beam, producing the bright features in the center of each raster scar. Scale bar is 500 µm.

5634

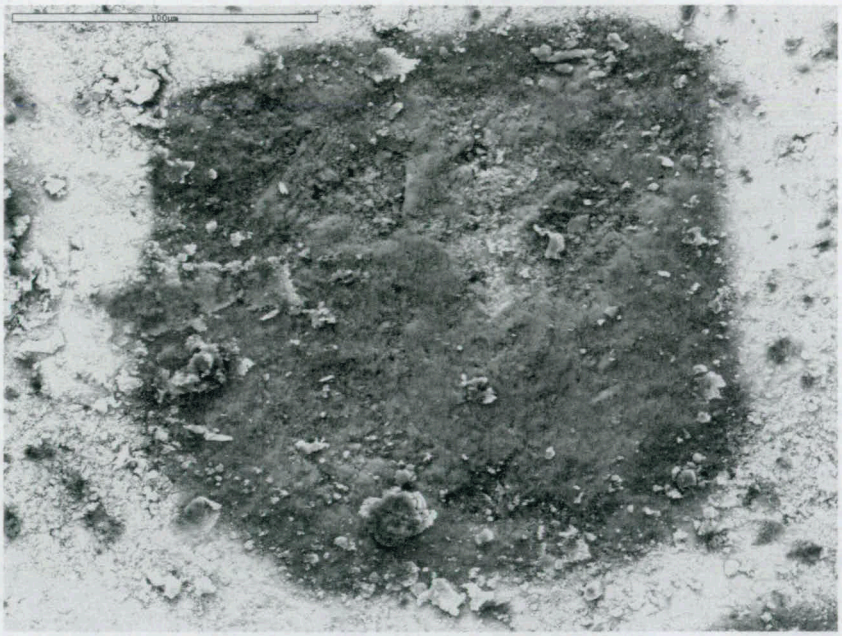

Figure 22. KD33262. BSE image of one of the depth profiling raster scars in Figure 18. Ion milling tends to selectively remove certain areas faster than others. Note pits in upper center of raster scar. On a rough surface the topography becomes exaggerated by ionization during the depth profiling. Scale bar is 100 µm.

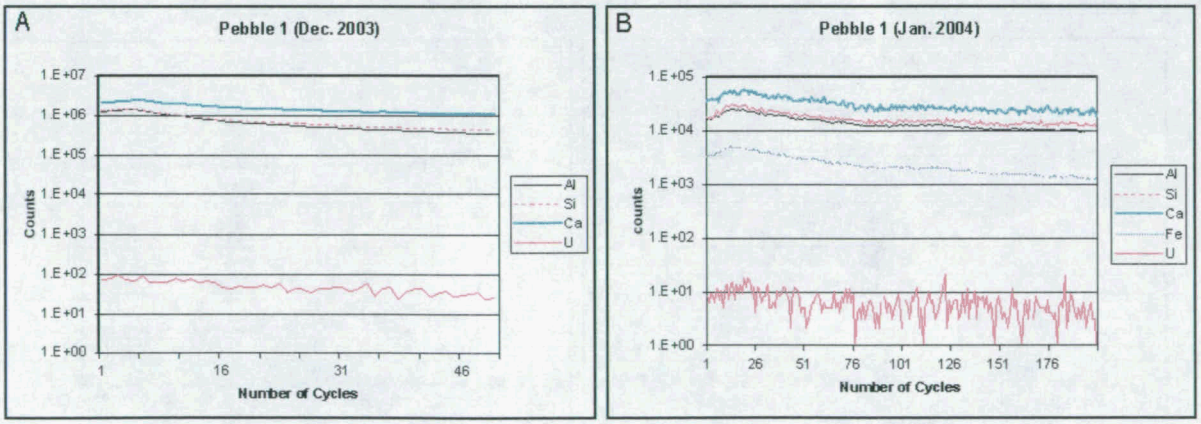

Figure 23. Depth profiles from two different areas of pebble 1 (calcite). Note different scales indicating higher beam current in A than B.

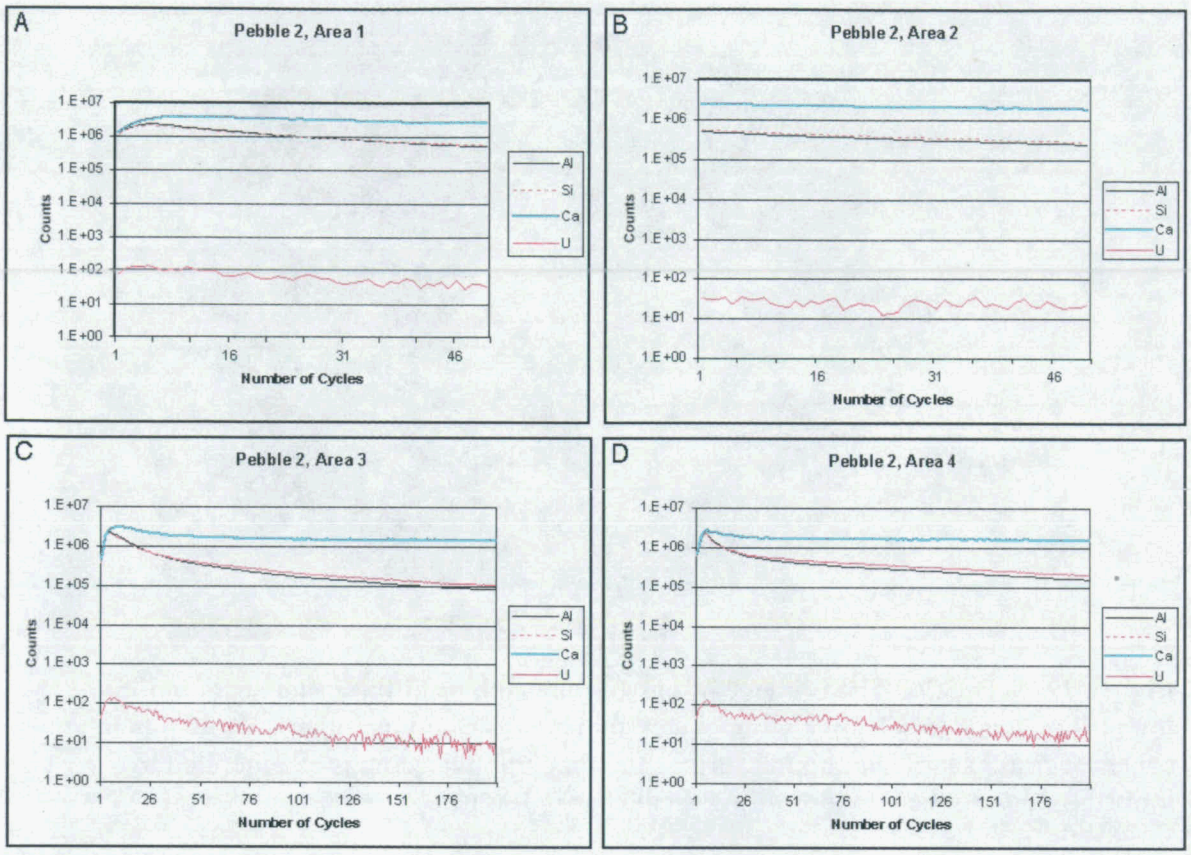

Figure 24. Depth profiles from four areas of pebble 2 (calcite).

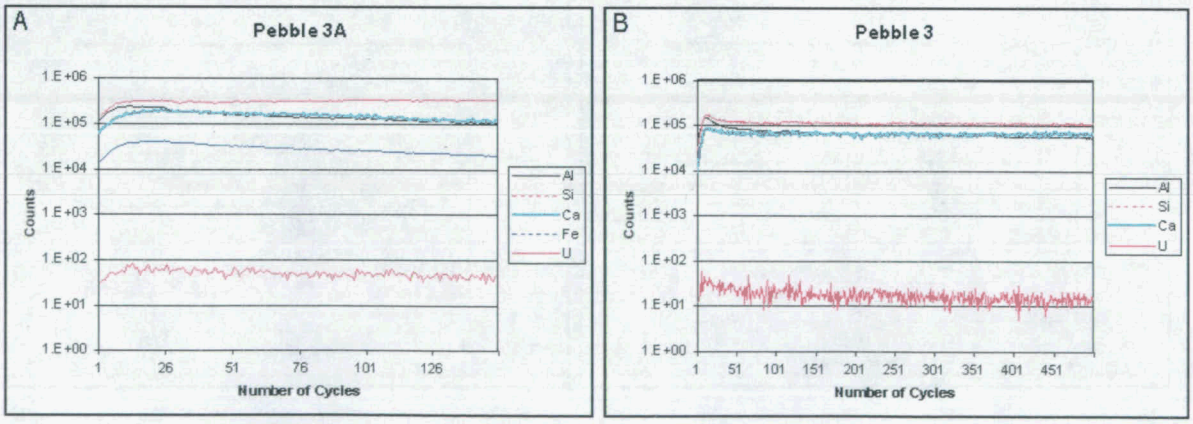

Figure 25. Depth profiles from two areas on pebble 3 (quartz).

5634

In the second calcite pebble, shown in Figure 24, Ca shows a rapid rise followed by a level or shallow slope in all plots, the result of Ca in the substrate. In area 3 and 4 (Figure 24C and D), Al and Si both have a strong initial peak followed by a rapid decline, an indication of significant clay on the surface. These two plots also show the most interesting results for uranium, which, like the Al and Si, shows an initial peak. The uranium plot declines to the right of the peak, paralleling the Al and Si. This parallel behavior may indicate that uranium is present with clay (containing Al and Si) that is on the surface. However, it is also possible that the uranium is associated with another fine-grained mineral phase mixed with the clay, and that the correlation with Al and Si is due to the presence of clay minerals in the fine-grained mixture. Note that in Figure 24D, the uranium plot is nearly level for some distance beyond the initial peak, to around 76 cycles, while the Al and Si drop off quickly, suggesting that the U may be associated with a different phase. Uranium in Figure 25A shows no peak and parallels the other elements Al, Ca and Fe. Silicon response is flat due to the high concentration in the quartz substrate. The plot in Figure 25B also shows an initial peak for Al, Si and U.

Washed pebbles. Figure 26 shows the results of depth profiling on two washed pebbles. The calcite pebble 2 was previously analyzed in the unwashed state using depth profiling (Figure 24). The same pebble was rinsed in deionized water, scrubbed with a soft brush, and rinsed in deionized water for 30 minutes in an ultrasonic cleaner, Pebble 5, a dolomite,

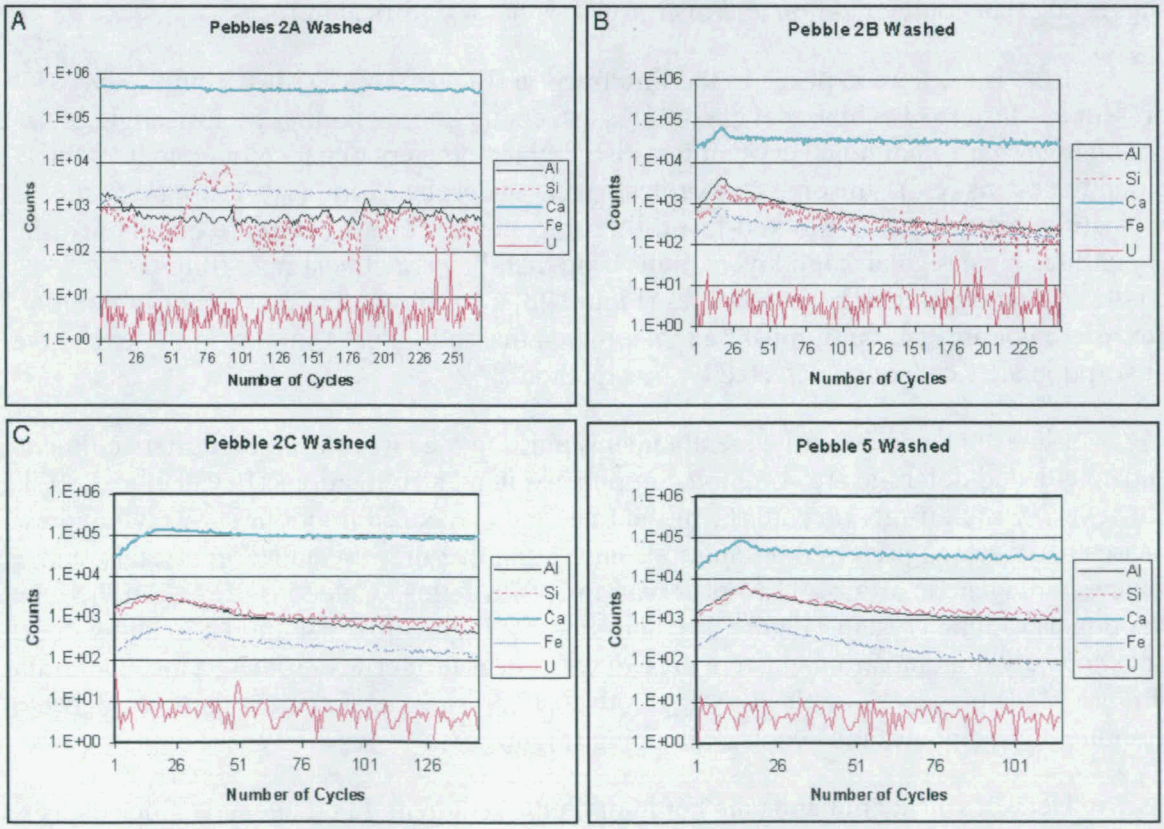

Figure 26. Depth profiling on pebble 2 after washing (A, B, and C) and on pebble 5 (D), also washed.

was rinsed for 5 minutes in deionized water in an ultrasonic cleaner. This treatment should not result in significant desorption of uranium from the grain surface.

Several things are evident in comparing Figure 24 with Figure 26. First is it apparent that Si and Al are much lower relative to Ca in Figure 26A, B and C, an indication that the adhering clay was mostly removed. There is evidence that some clay does remain in some areas, as there is still an initial peak of Al and Si (Figure 26B). The second important feature is that uranium shows no initial peak as it did in Figure 24C and D. This may indicate that the uranium has been removed. Likewise in pebble 5 (Figure 26D) there is no initial U peak and the background counts are low, indicating that there is no uranium on the grain surface.

4.2.3 TEM analysis

The fine-grained fraction of the sediment consists of several phases. Several minerals were identified by a combination of TEM, selected-area electron diffraction (SAED), X-ray energy-dispersive spectroscopy (EDS), and high-angle annular dark-field imaging (Z-contrast imaging) techniques. Identified minerals include illite/smectite, calcite, dolomite, gypsum, apatite, iron oxyhydroxide, quartz, albite, and anatase. Many of these are present as euhedral crystals, indicating that they formed diagenetically, and could potentially permanently sequester uranium through incorporation into the crystal structure, or by surface coprecipitation and overgrowth. However, although Z-contrast imaging is capable of resolving uranium phases as small as 5-10 atoms, no such phase was observed, suggesting that coprecipitation and overgrowth is not a significant process.

Illite is a common phase in the fine fraction (Figure 27, a-f). It is commonly present as clusters of subparallel crystallites (a), contacting each other by low-angle grain boundaries (b,d). Individual crystallites are a few nanometers to tens of nanometers thick along the c-axis (c,d). In some crystallites, layers wider than 1 nm (10 Å) are present, indicating that the clay is a mixed-layer illite/smectite (e). However, more commonly, the crystallites have regular 1 nm layers, indicating that they are almost pure illite (f). Z-contrast imaging of the clay crystallites (Figure 28, a-b), shows that clusters of uranium atoms are not present, but it must be remembered that individual U atoms in ion-exchange or sorption sites cannot be detected by this method.

Limestone and dolomite are abundant lithics in the Great Miami Aquifer sediments, and calcite and dolomite are common components in all size fractions (Bryan et al. 2003). However, X-ray diffraction patterns of the fine- and clay-sized fractions showed that these phases had a strong preferred orientation, suggesting that they are euhedral crystals, and hence, of diagenetic origin. TEM observations confirm this. Calcite is present in the fine fraction as rodlike crystals (Figure 29), and rhombs (Figure 30). Z-contrast imaging does not show any uranium atom clusters present on of near the surface of the grains. Dolomite (Figure 31) is present as tooth-like "dogtooth spar" crystals, again, showing no evidence of uranium coprecipitates in Z-contrast imaging (Figure 32).

Detrital silicate minerals are common in the sediment, but diagenetic silicates were also identified in the fine fraction. Quartz is present in the form of euhedral crystals (Figure 33, 34), and albite with crystal faces is also present (Figure 35).

5634

Diagenetic apatite is present as well, as clusters of euhedral crystals (Figure 36). The apatite is probably due to release of phosphorus from chitinophosphatic fossils in the limestone and dolomite lithics which comprise most of the sediment. Although apatite is known to sequester uranium, it is unlikely to be forming in large enough amounts to contribute significantly to binding uranium in these sediments.

Diagenetic anatase is present as clusters of 50 nm crystallites (Figure 37), and probably forms as a weathering product of biotite and other detrital igneous/metamorphic ferromagnesian minerals. Anhydrite was also identified (Figure 38)—probably forming by dehydration of gypsum in the vacuum of the TEM. As the groundwater is unsaturated with respect to gypsum, it is likely that this formed when the sediment sample was dried for analysis.

Also present in the fine fraction, and in the grain coatings, is poorly crystalline iron oxy-hydroxide, ferrihydrite. This occurs as clusters of either ball-like or rod-like crystallites (Figure 39), occasionally with needlelike crystals of lepidocrocite (Figure 40). Ferrihydrite has a high surface area (source), and strongly, perhaps irreversibly, sorbs uranium and other metals. EDS analysis of ferrihydrite in the Fernald sediments shows measurable levels of Pb and Mo (Figure 41), and a small fraction of the uranium present in the sediments was shown to be associated with amorphous iron oxy-hydroxides in Phase I of this study (Bryan et al., 2003), and to be very strongly, perhaps irreversibly sorbed. However, uranium was not observed in the ferrihydrite by EDS, and, because the aquifer is oxidizing, the amount of iron oxyhydroxide present is very small. It is unlikely that much of the uranium is tied up in this material.

The sample containing wood fragments was also examined. Ferrihydrite was commonly associated with dark brown wood fragments in soil samples. Pyrite occurs as large euhedral crystals up to larger than one micron, or as a component of "framboidal pyrites." "Framboidal pyrites" are closely associated with wood twigs (Figures 42, 43), and consist of clusters of euhedral, ~100 nm diameter crystals, commonly showing an ordered arrangement. Uranium was not observed in any samples, but is assumed to be concentrated in the wood fragments by reduction and precipitation as a U(IV) phase.

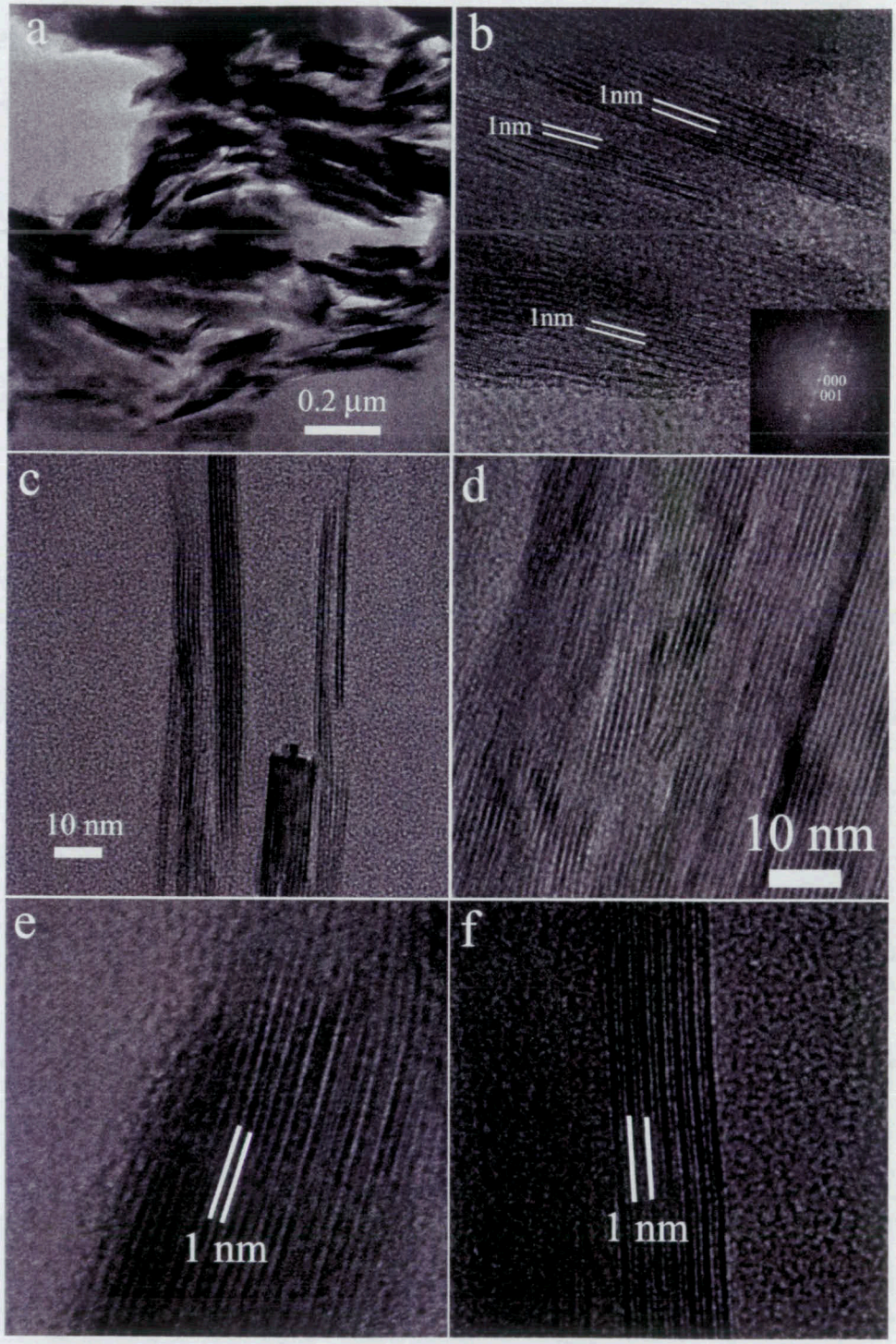

Figure 27. TEM images of illite and illite/smectite. **(a)** Bright-field low magnification TEM image of illite/smectite pack. **(b, c, d, e, and f)** HRTEM images of illite and illite/smectite; (b,d) low-angle grain boundaries between crystallites; (c,d) illite crystallites vary in thickness from <10 nm to 10's of nm; (e) mixed layer illite/smectite shows variability in layer thickness; (f) nearly pure illite shows only 1 nm layers.

5634

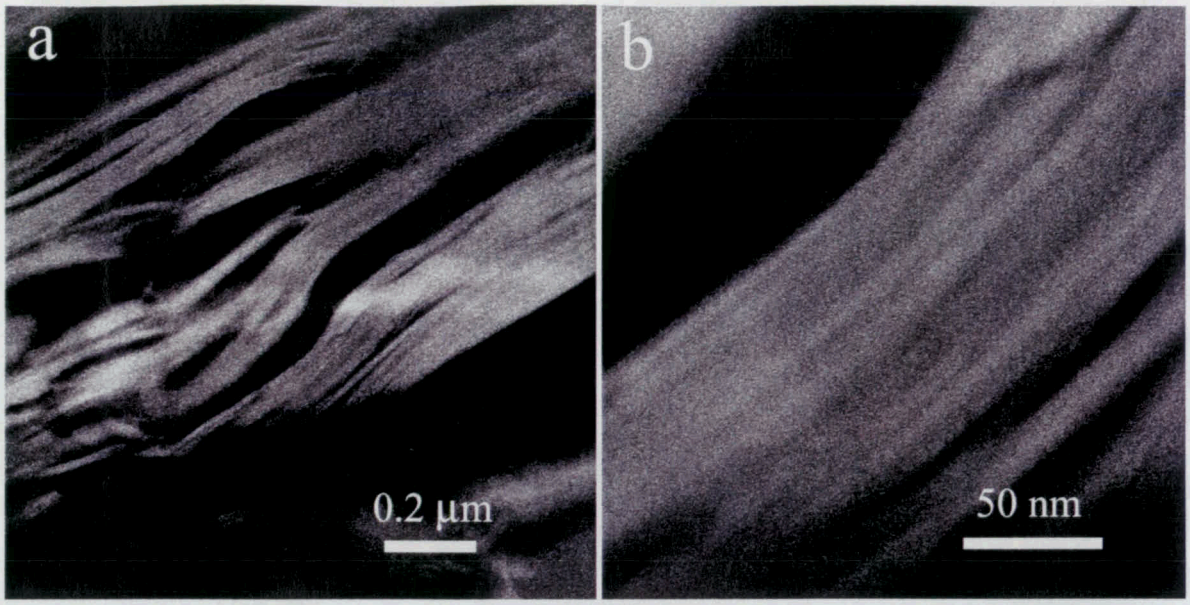

Figure 28. Z-contrast images of illite. **(a)** low magnification. **(b)** higher magnification.

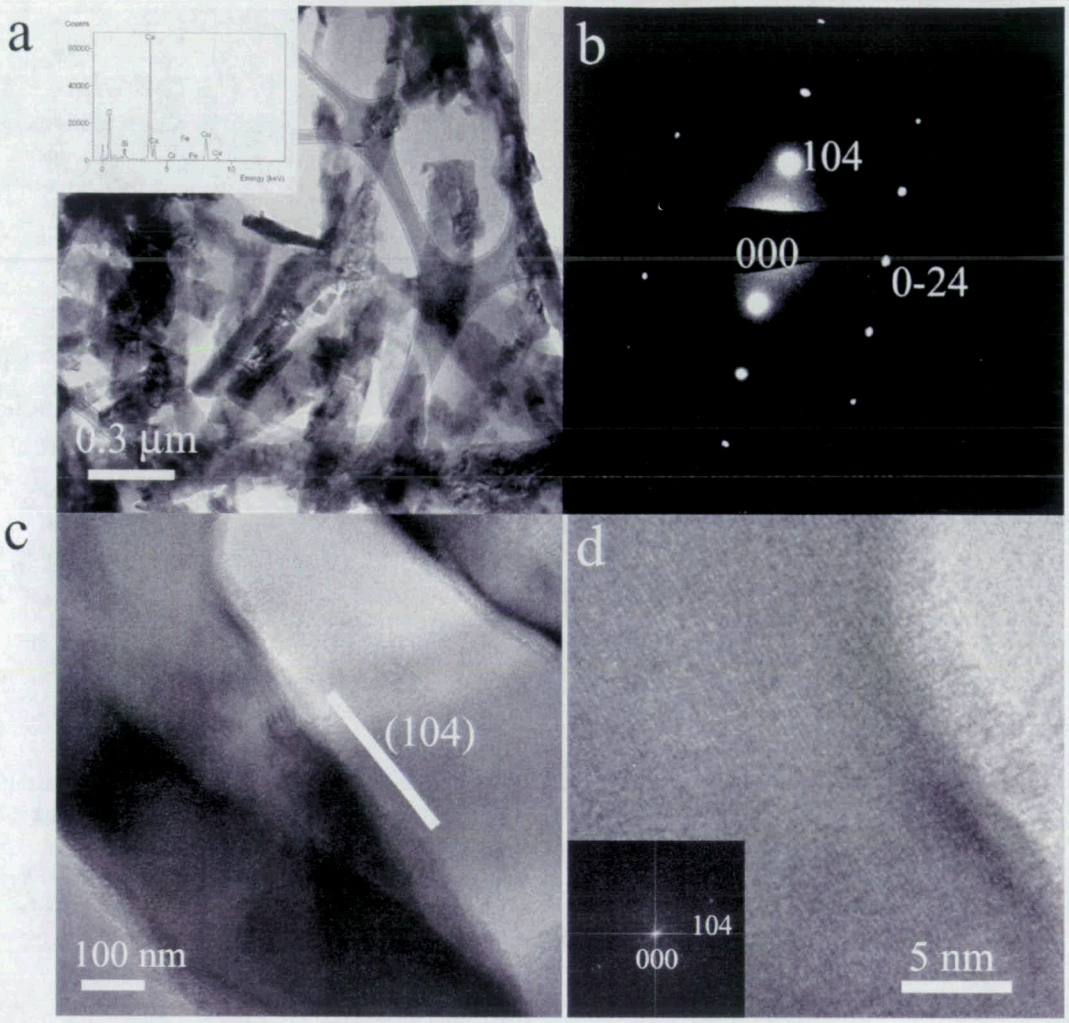

Figure 29. TEM images of rod-like calcite. (**a**). Bright-field low magnification TEM image. (**b**). selected area electron diffraction (SAED) pattern. (**c**). Close-up TEM image of a rod-like calcite. (**d**). The corresponding HRTEM image and the FFT pattern (inserted).

5634

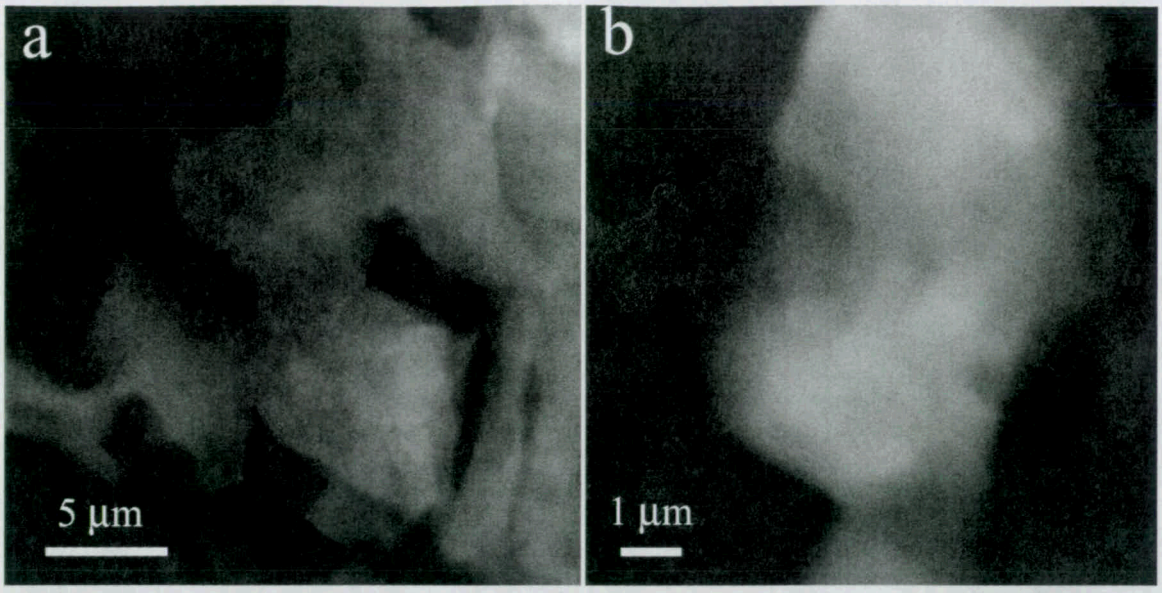

Figure 30. Z-contrast images of calcite. (**a**). low magnification image. (**b**). higher magnification image.

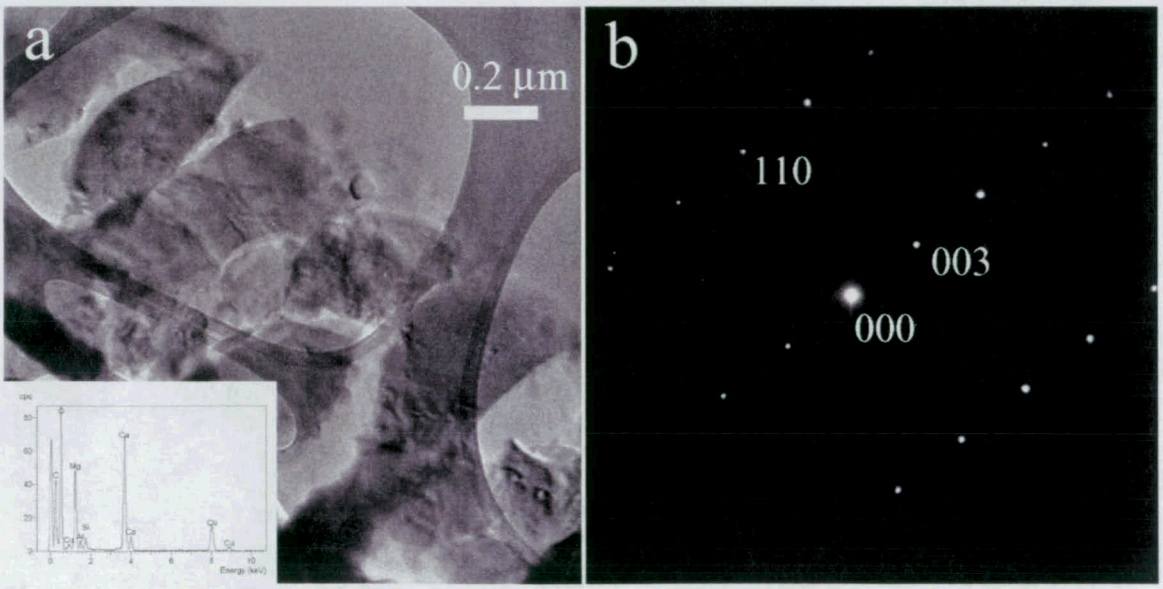

Figure 31. TEM images of dolomite. (**a**). Bright-field low magnification TEM of teeth-like dolomites. EDS result was inserted at the bottom left corner. (**b**). the corresponding SAED pattern.

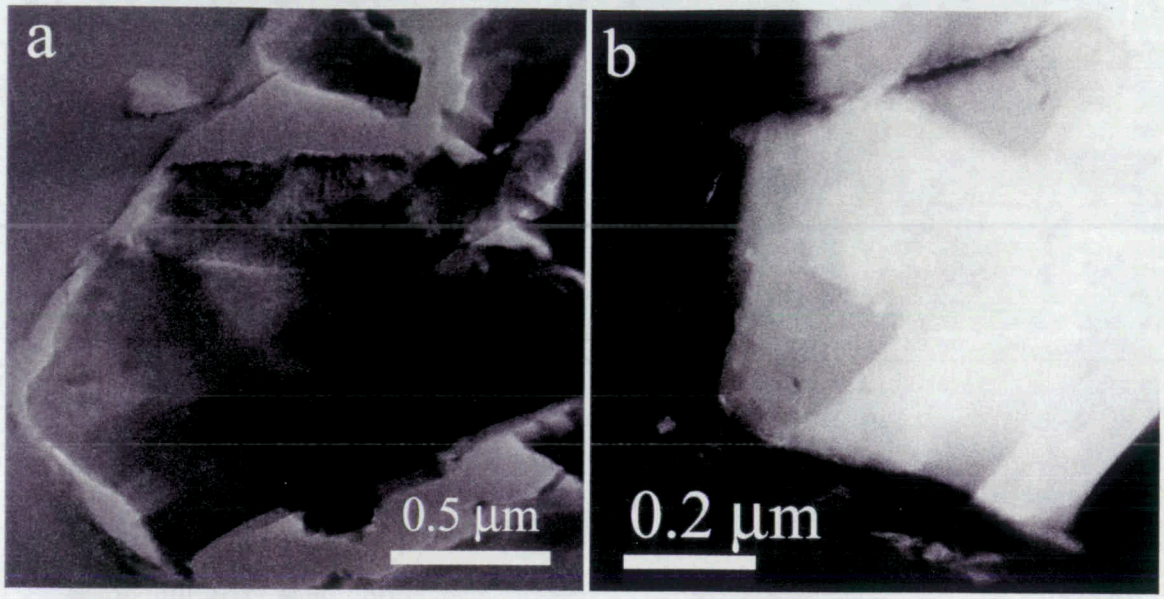

Figure 32. TEM (a) and the Z-contrast (b) images of dolomite.

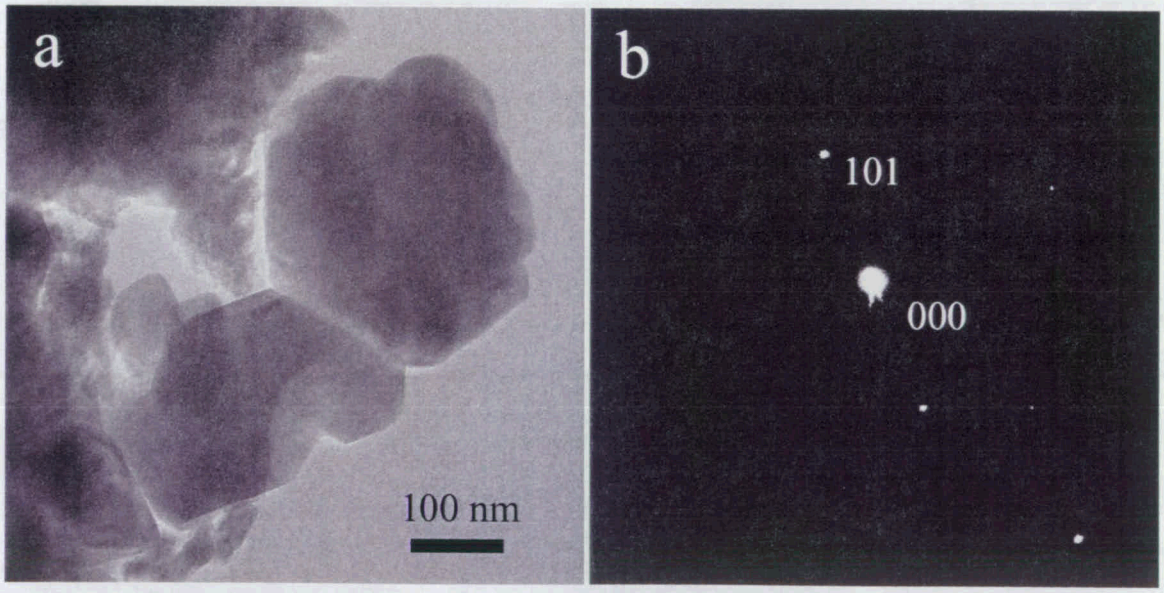

Figure 33. TEM images of quartz. **(a)**. Bright-field low magnification TEM image of euhedral quartz. **(b)**. The corresponding SAED pattern.

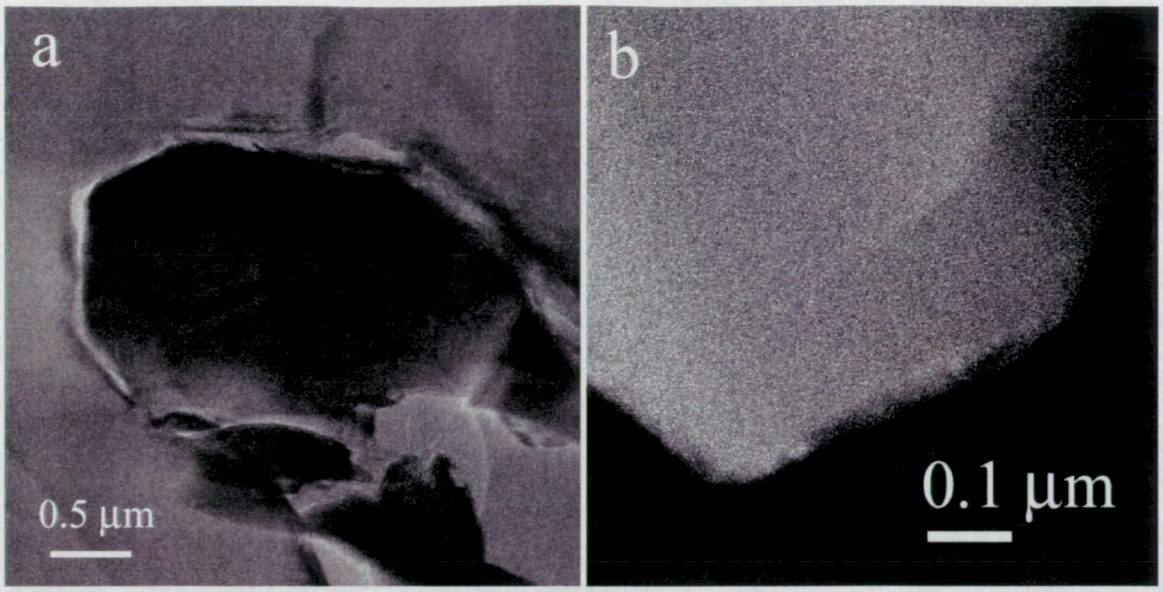

Figure 34. TEM (a) and the Z-contrast (b) images of quartz.

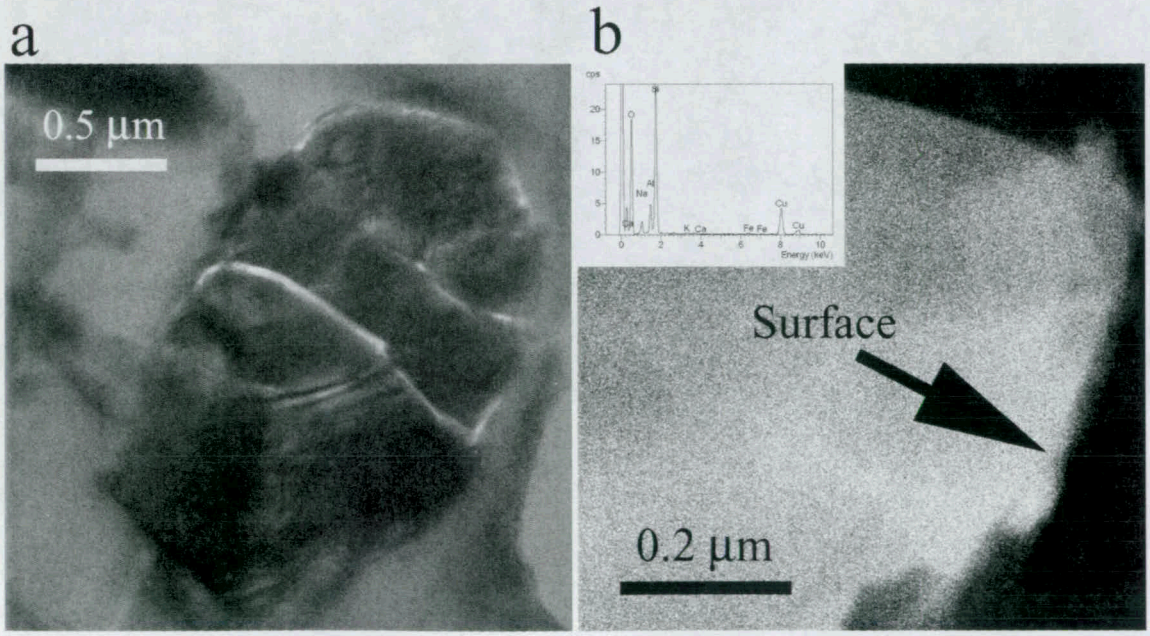

Figure 35. TEM (a) and the Z-contrast (b) images of albite. EDS spectrum was inserted at the top left corner in b.

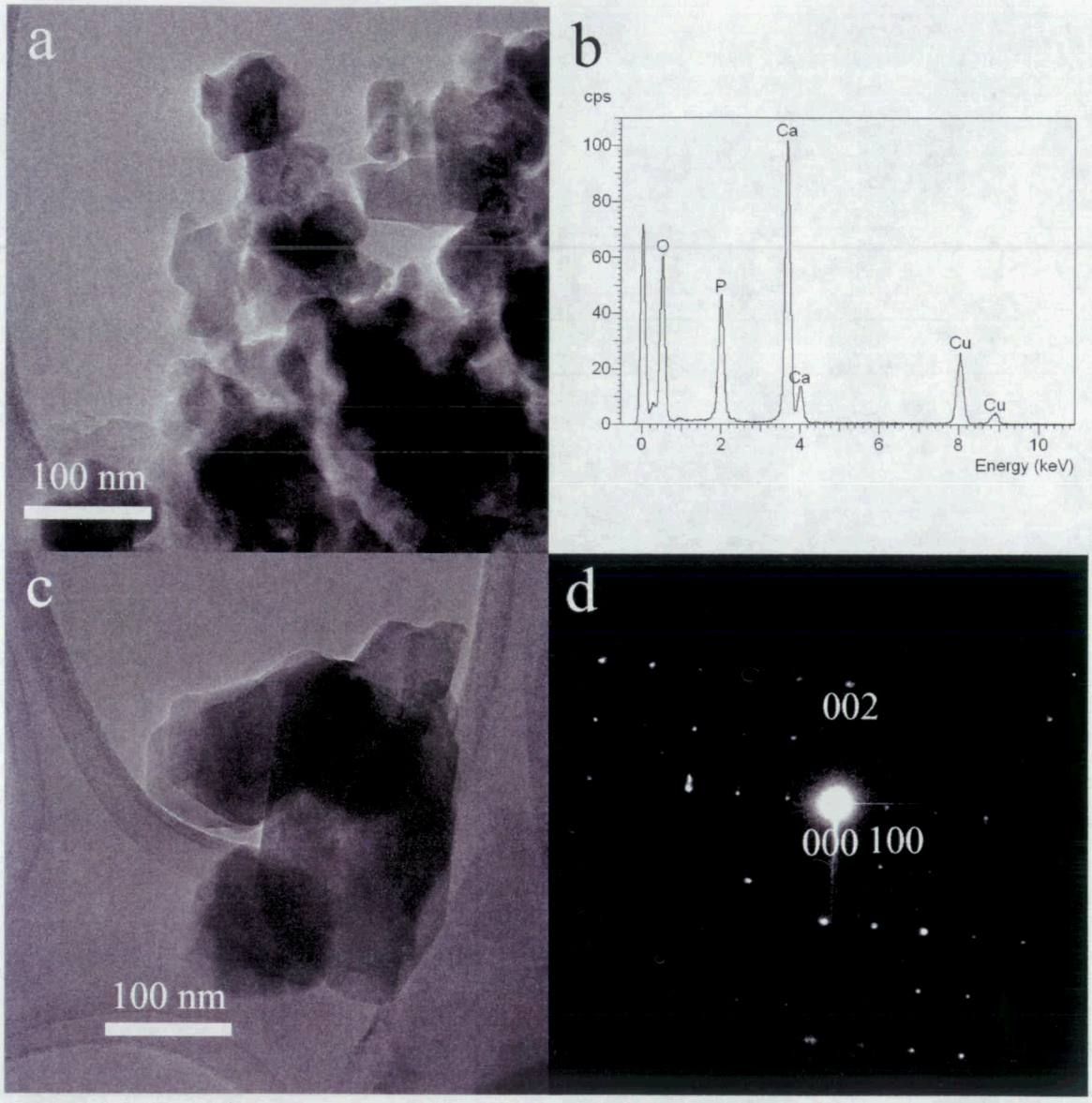

Figure 36. TEM image of apatite and EDS results. (**a**). Bright-field low magnification TEM image of apatite aggregate. (**b**). EDS spectrum. (**c**). Bright-field low magnification TEM of apatite grains. (**d**). the corresponding [010] SAED pattern.

5634

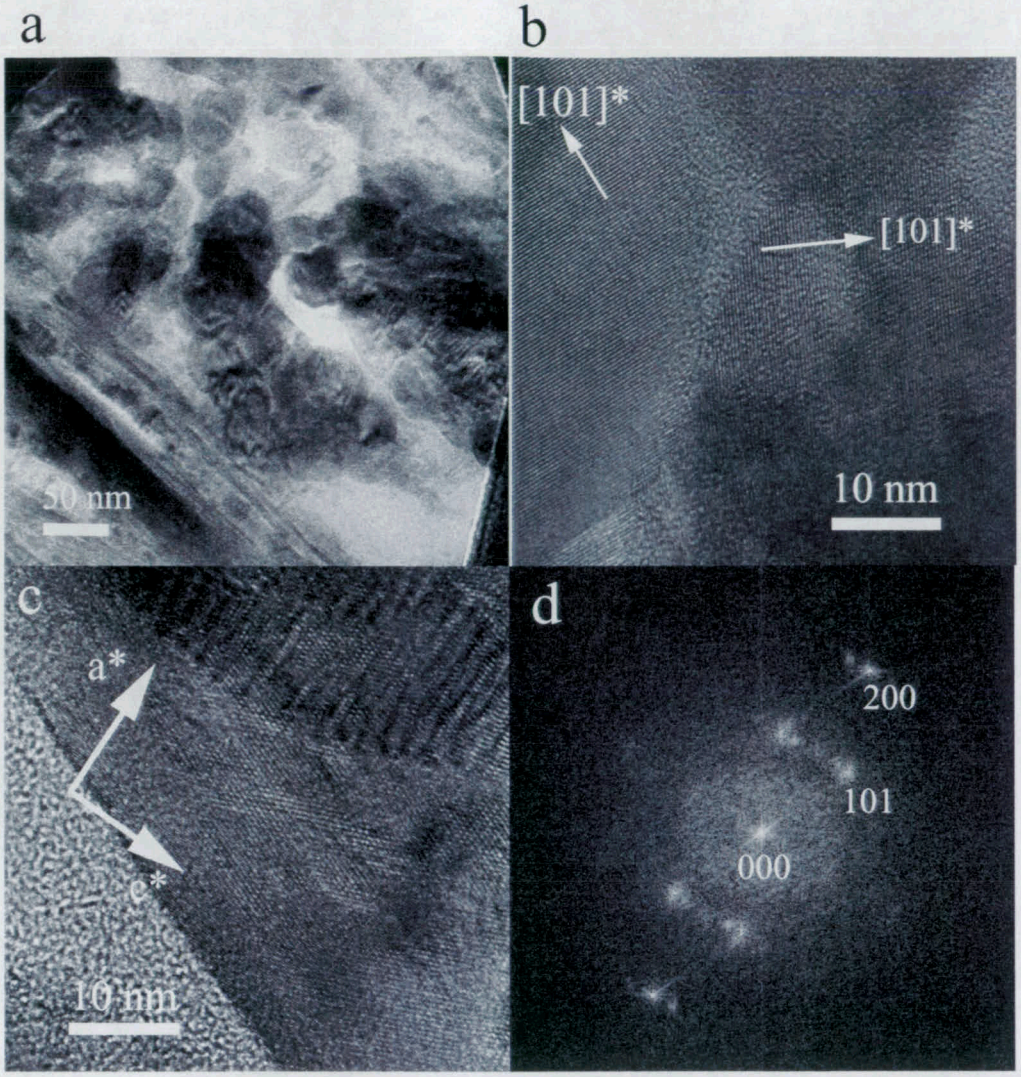

Figure 37. TEM image of anatase. (**a**). Bright-field low magnification TEM image of anatase aggregate. (**b**). HRTEM image of anatase grains, indicating that the aggregate provides several ten nanometer pores. (**c**). [010] HRTEM image of anatase. (**d**). The corresponding FFT pattern.

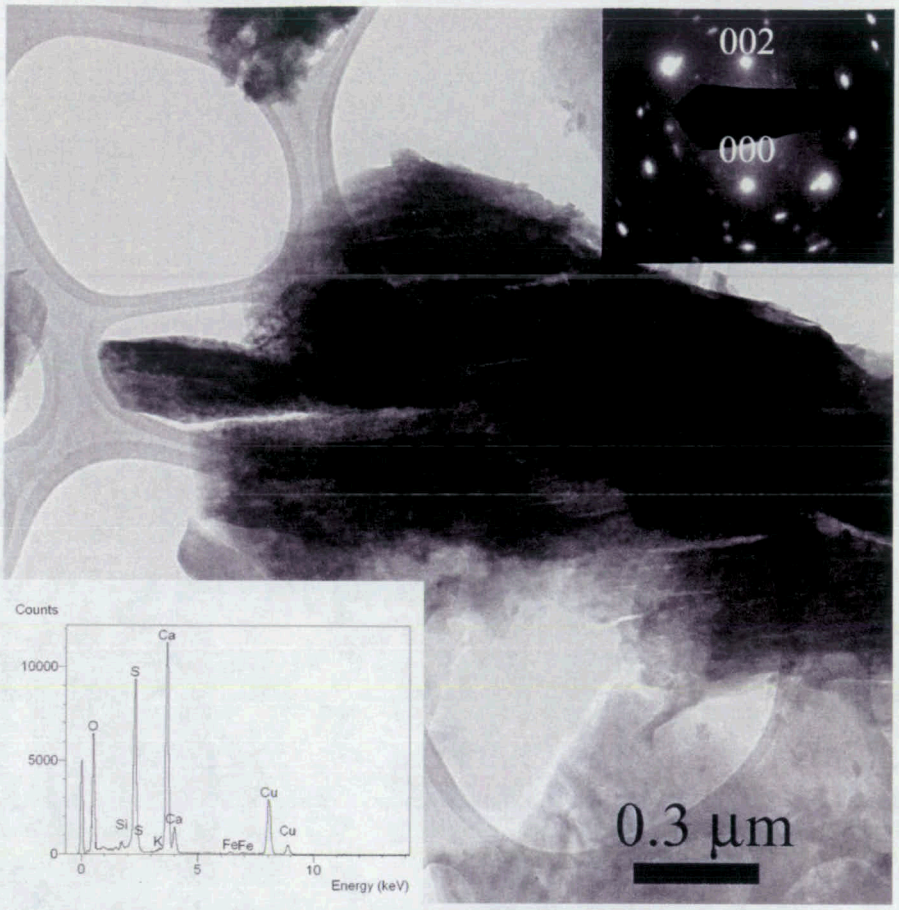

Figure 38. TEM image of anhydrite. SAED pattern (top right) matches that of anhydrite, but the anhydrite may be a transformed product of gypsum in electron microscope. EDS spectrum was inserted at the bottom left corner.

5034

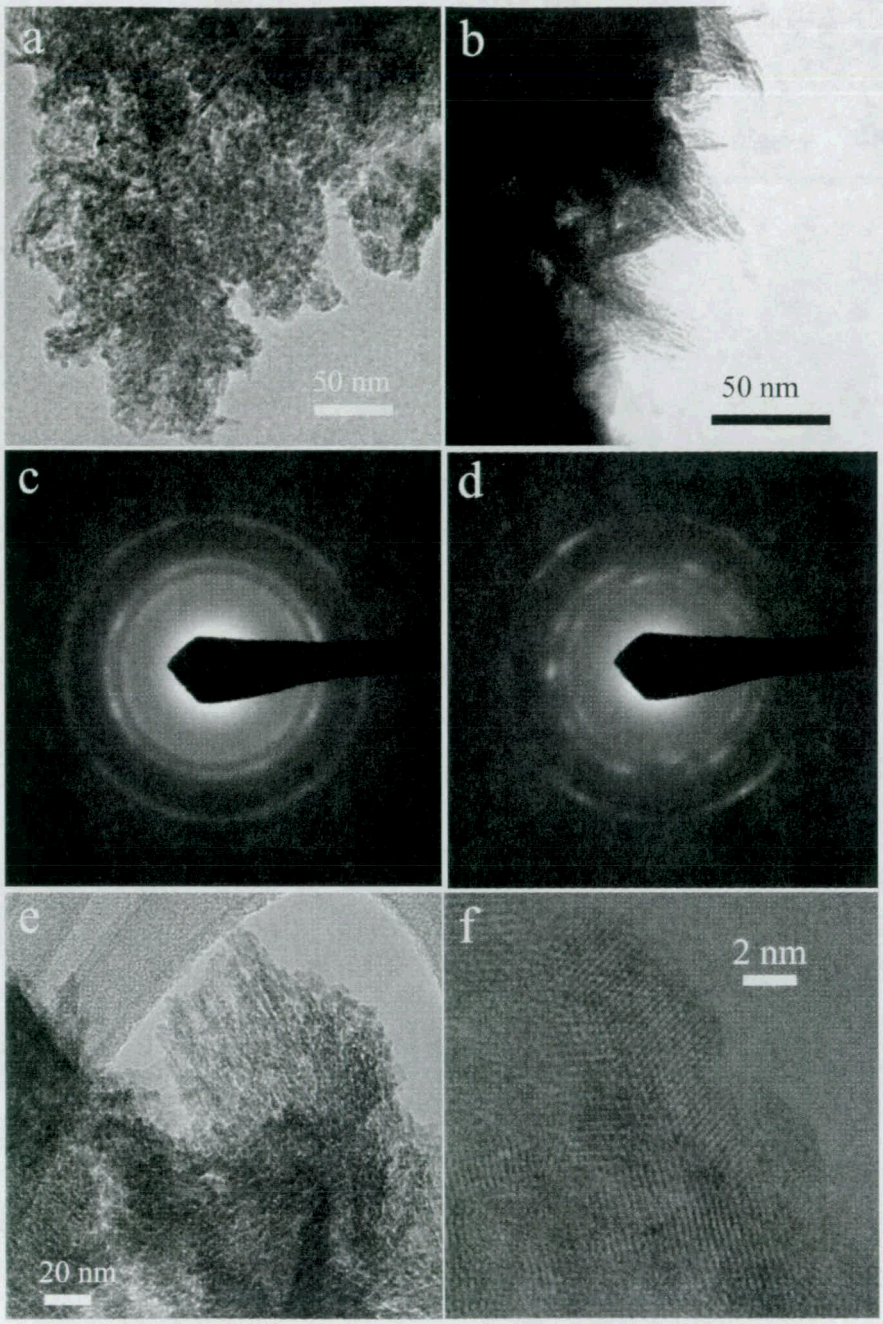

Figure 39. TEM images of ferrihydrite. **(a) and (b)**. Bright-field low magnification TEM images of ferrihydrites aggregate. They show ball-like (a) or rod-like (b) shapes. **(c) and (d)**. SAED patterns corresponding to (a) and (b). The SAED of ball-like particles shows ring pattern, suggesting highly random orientations. The SAED of rod-like particles shows imperfect ring pattern, suggesting that some rod-like particles have similar orientations. **(e)**. Another example of rod-like particles. **(f)**. HRTEM image of rod-like particles.

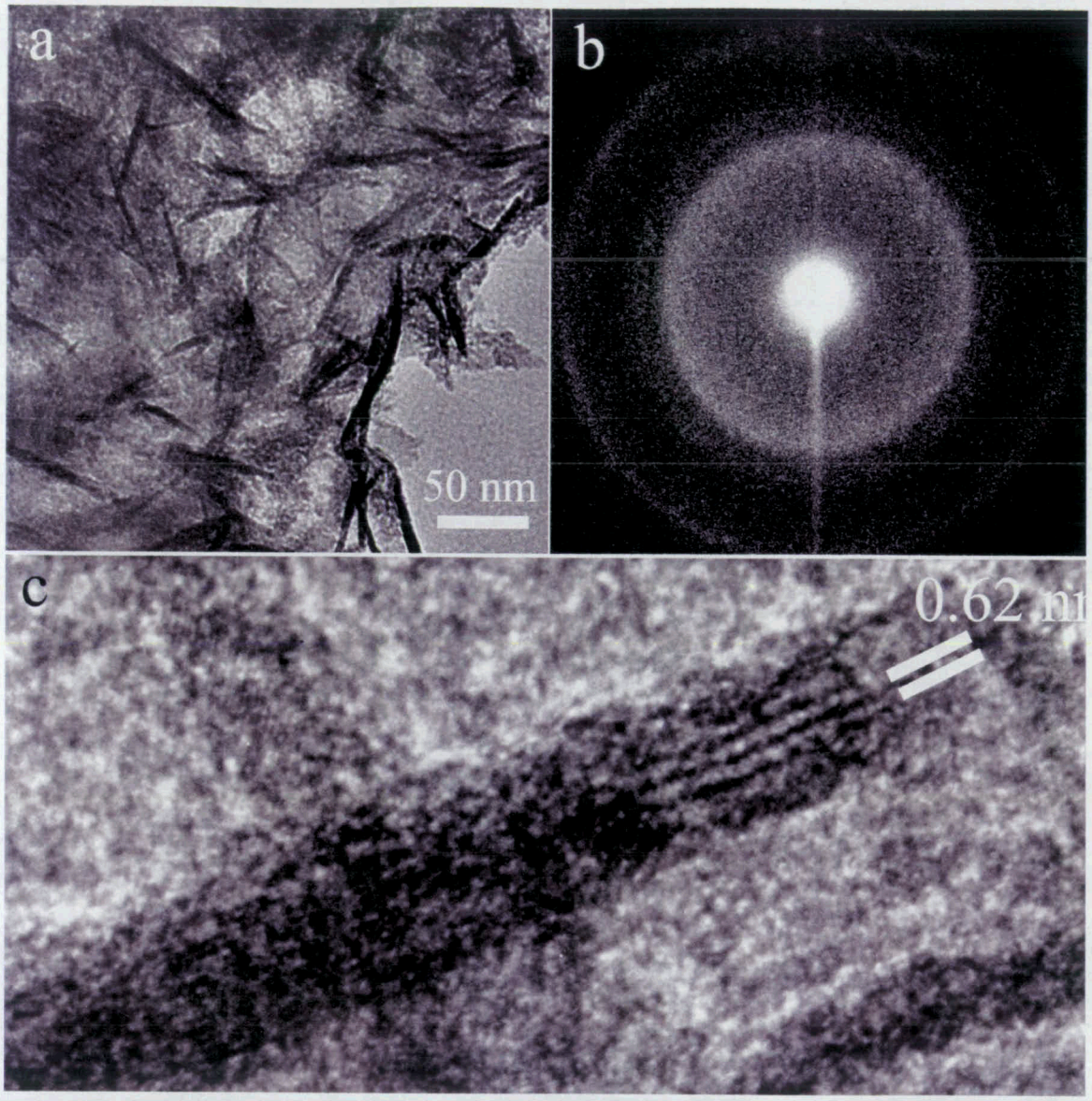

Figure 40. TEM images of ferrihydrite and lepidocrocite. (**a**). Bright-field low magnification TEM image of ferrihydrite and lepidocrocite aggregate. Lepidocrocite shows a needle like shape in the image. (**b**). SAED pattern of the aggregate. (**c**). HRTEM image of lepidocrocite, showing 0.62 nm or 0.31 nm lattice fringes.

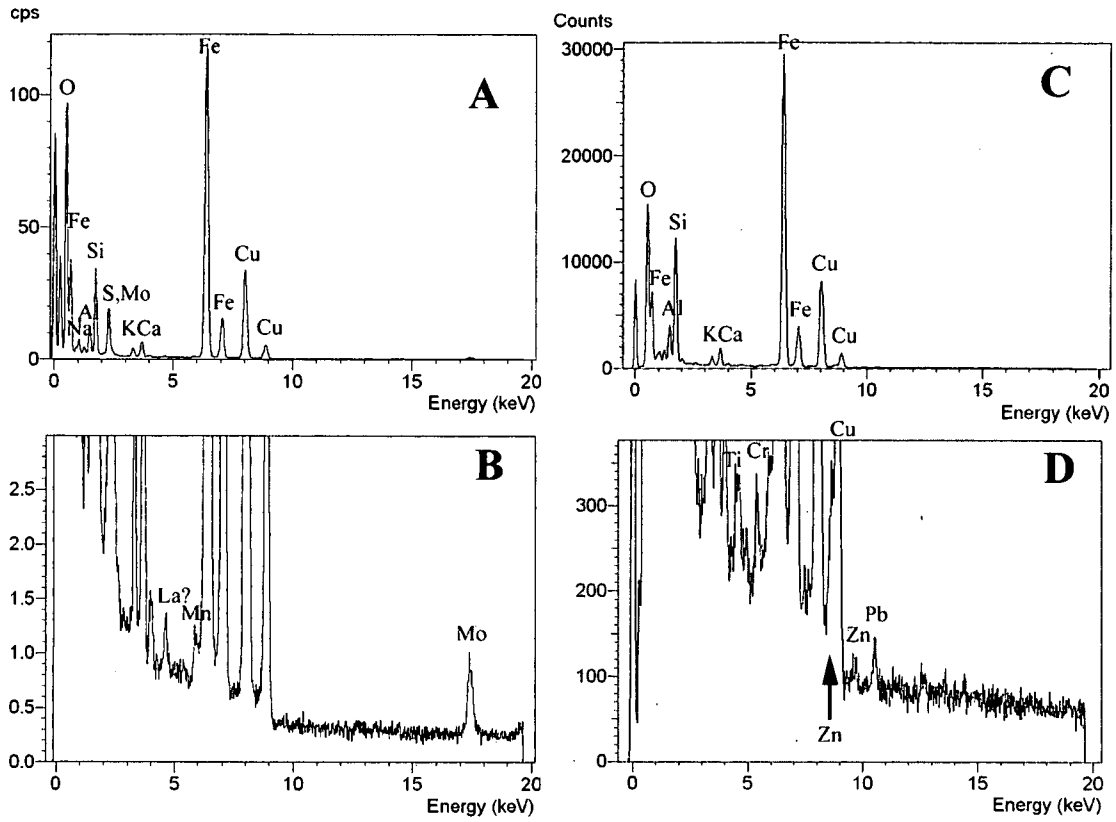

Figure 41. EDS spectrum of Mo-bearing (A, B) and Pb-bearing (C, D) ferrihydrite.

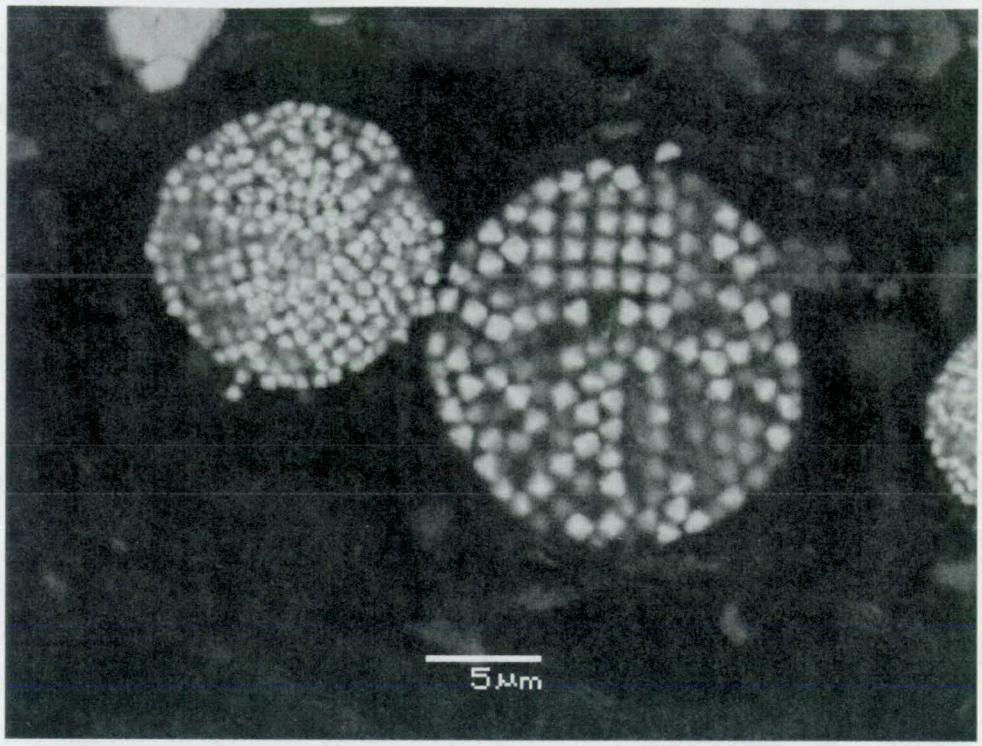

Figure 42. SEM secondary electron image of a globular cluster of pyrite octahedrons in a sample of wood recovered from borehole KD33298, at a depth of 66'–66.5'. The ordered arrangement of the pyrite octahedrons suggests that their nucleation may have been microbially-mediated.

5634

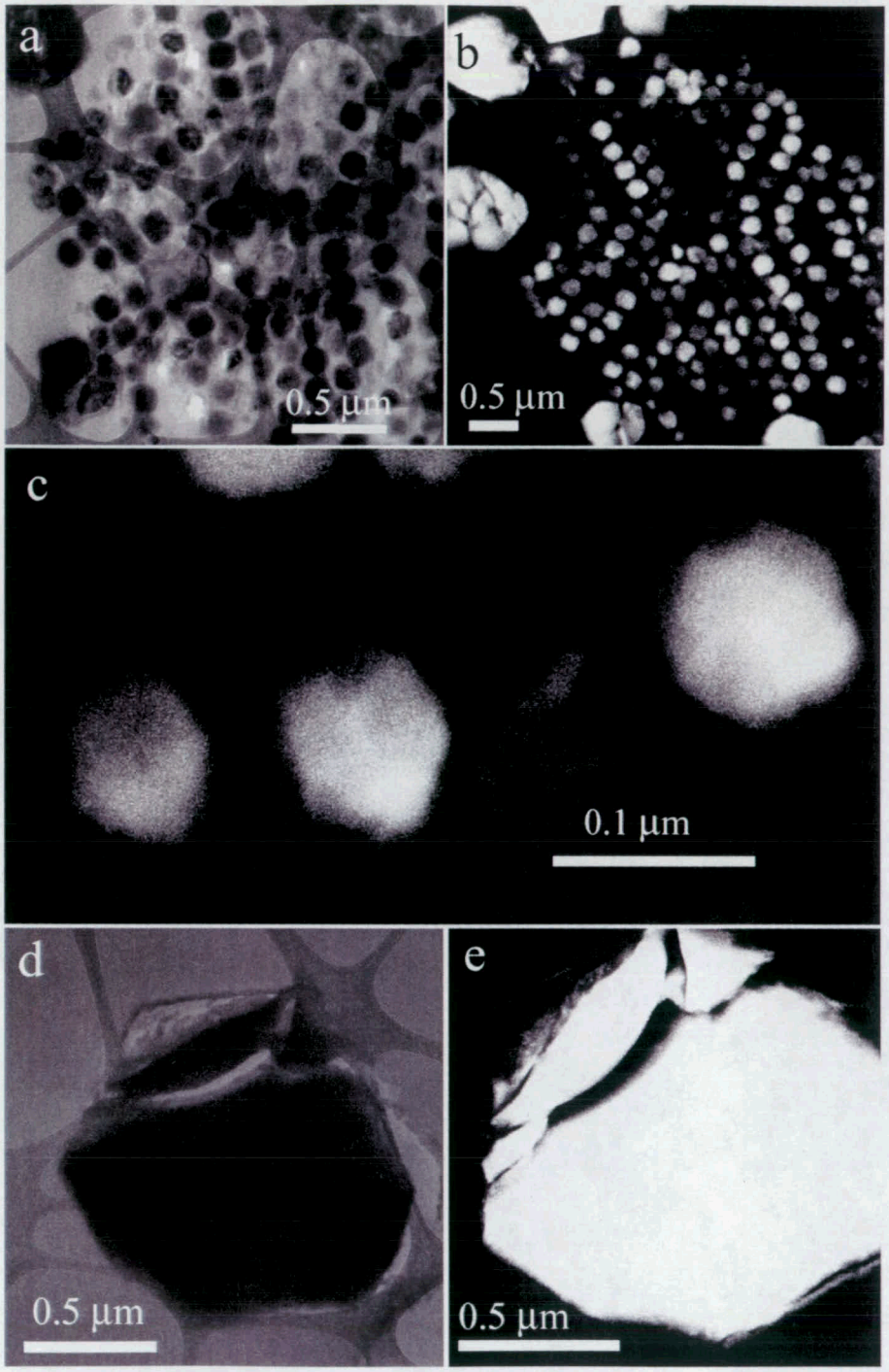

Figure 43. TEM image of pyrite. (**a**) Bright-field low magnification TEM of framboidal pyrite. It is composed of euhedral pyrite with ~100 nm size. (**b**). The Z-contrast image. (**c**). The Z-contrast image of pyrite particles at a higher magnification. (**d**). Bright-field low magnification TEM image of a pyrite grain having ~1 um size. (**e**). The Z-contrast image of the pyrite.

This Page Intentionally Left Blank

5. Summary

In Phase I of this study (Bryan et al., 2003), sediment samples from the uranium contaminant plume in the Great Miami Aquifer, beneath the DOE Fernald site, were analyzed using sequential extraction analysis. This procedure yielded information on how the uranium is partitioned between the minerals in the aquifer sediments and allowed evaluation of the mobility of the uranium—what fraction of the whole is labile, and what fraction is sequestered in mineral structures or by mineral overgrowth and encapsulation. The results of that study showed that whole-rock uranium concentrations in the shallow, uncontaminated samples averaged 1.4 μg/g, the background concentration. Samples from the contaminant plume had higher U concentrations, with a maximum of 5.88 μg/g. Some was present in readily exchangeable sites, loosely sorbed onto mineral surfaces (outer sphere), and possibly in clay interlayers. The largest fraction, however, is associated with carbonate minerals. Much of this is present on the mineral surface and is labile, but a significant fraction, perhaps as much as half, is not readily displaced and may be sequestered in the mineral structure. The amount of uranium associated with amorphous and crystalline iron oxides is minor. The remainder of the uranium, comparable to the amount present in the uncontaminated sediments is bound in insoluble and nonreactive minerals, and is immobile.

Although little uranium is bound to organic material in the bulk sediment samples, fragments of wood isolated from the sediment contain high concentrations of uranium. Wood in the aquifer probably concentrates uranium through microbially-mediated reduction and precipitation processes.

In Phase II of this study, samples of contaminated sediment have been further characterized to evaluate the relative fractions of labile and fixed uranium present. In addition, wood fragments from the aquifer, concentrated in uranium relative to the surrounding sediment, have been examined to determine the form and location of the uranium in the wood.

A series of batch sorption/desorption experiments have been carried out to determine the fraction of mobile uranium in the sediments. These experiments were not wholly successful, due to the problem of CO_2 degassing from the groundwater over the course of the experiments. Carbonate strongly complexes uranyl, increasing its stability in solutions. In the batch experiments, the uranium concentrations were highest in the initial sample aliquot, and decreased with time as the solutions degassed and the carbonate concentration dropped.

Because of the degassing, it is difficult to determine the amount of labile uranium present. Using the initial samples collected, before any degassing has occurred, and correcting for desorption kinetics, indicates that a Kd of ~8.7 mL/g is appropriate for time intervals relevant to remediation, if none of the contaminant uranium is fixed (not exchangeable). However, the sorption data suggest that a significant amount of the uranium (perhaps as much as 65%) is fixed or at least slowly desorbing, and a more appropriate K_d, for the mobile fraction, may be ~2.8 mL/g.

Finding exactly how the uranium is hosted on the submicron scale is a challenging technical problem. Detection of uranium in these sediments using microanalytical methods also proved to be difficult, although, given the very low concentrations of uranium in the sediments, this was not unexpected. The concentration of uranium in the contaminated sediment is 5.88 μg/g, and concentrations in the oxidized, carbonate-rich groundwater of the contaminant plume are up to a few hundred μg/L—well below solubility limits for uranyl minerals. Thus, uranium phases were not expected in the sediments, and even with Z-contrast imaging by high-resolution transmission electron microscope (HR-TEM), capable of observing clusters of uranium as small as 5-10 atoms, no such phases were found. This strongly suggests that uranium is not present as a discrete phase or coprecipitate, and indicates that uranium is not likely to be sequestered by coprecipitation as a discrete phase onto mineral surfaces and mineral overgrowth.

Two clear associations of uranium were observed in these samples. One association is of uranium with clays and other fine-grained materials in pockets on sand-sized grains. The other association is that of uranium and pyrite. Concentrations of uranium are found in younger pyrite overgrowths on older pyrite.

Uranium was observed using secondary ion mass spectrometry (SIMS), in concentrations up to 150 μg/g in the fine (clay-sized) fraction of the sediment. Concentrations appeared to be highest in fine materials adhering to larger grain surfaces. The large grains themselves are generally low in uranium: quartz sand contains no internal uranium, but a few μg/g of uranium was measured internally in detrital calcite grains. Both elemental ion probe analyses and depth profiling was able to detect uranium in these areas, but because of the large size of the ion beam, exactly where the element is could not be determined. Several different phases are usually present within these pockets: 1) layered silicates such as illite, smectite, or chlorite, as determined by EDS; 2) quartz and feldspar; 3) calcite and dolomite, 4) Fe- and Ti-oxides. Several potential hosts for uranium are present. Uranium could be sorbed to iron oxides, since they are efficient getters of uranium. Likewise, uranium may be sequestered into clay interlayer sites. Much of the clay and Fe-oxides are authigenic and probably strongly attached to the larger sand and pebble grains. Uranium can then be strongly sorbed by this submicron material. Finally uranium could be bound to the surfaces of carbonate minerals, including the micrometer-sized particles within the clay pockets and the surfaces of larger carbonate sand and pebbles.

Certainly, there is a correlation between U and Al in some of the elemental maps done on the electron microprobe (Figure 9) and between U, Al and Si in the depth profiles (Figure 24). This could suggest that the U is associated with clay minerals. However, the highest concentrations of U measured by electron microprobe (~100 μg/g; barely detectible) were measured on areas of fine-grained material containing dolomite. Also, in some depth profiles (e.g. Figure 24, area 4), the correlation between Al and U was poor. Thus, uranium may be associated with another phase mixed with clays in the fine-grained material. In Phase I of this study, characterization by sequential leaching indicated that most of the uranium is associated with carbonates. Also in Phase I, carbonate was found to be common in the fine-grained fractions of the sediments, and in this study, both calcite and dolomite were identified by HR-TEM as sub-micron crystals in the sediment. Thus,

carbonates still seem to the most likely candidate to be hosting the uranium in these sediments.

In samples containing wood, a significant amount of uranium is present in pyrite. The highest concentrations are in small framboids at the periphery of clusters of pyrite and also in overgrowths on larger framboids. The overgrowths are very irregular and are probably late precipitated pyrite.

The occurrence of pyrite in these samples is limited to the wood, where it is present as scattered framboidal masses within cracks and recesses in the large wood pieces or as crusts and layers on the smaller twigs. Framboidal pyrite is generally thought to be microbially mediated (Tebo et al., 1997). The wood provides a source of organic matter and maintains locally anaerobic conditions favorable to sulfate reducing bacteria. In this case, microbial reduction of sulfate to sulfide takes place in the anoxic environment within the wood. Both sulfate, probably in solution in the ground water, and a source of reduced carbon is required for this microbial reaction. The sulfate provides an electron acceptor and is reduced to S^{2-}. Hydrogen sulfide (H_2S) is commonly the product of the reaction and may have been present in the aquifer, but there is no evidence of that now. At least some of the sulfide was incorporated with iron to form Fe-sulfide, the iron itself likely removed from solution by microbial action, resulting in the deposition of the framboidal pyrite by the microbes. Sulfide production of mackinawite, pyrite, and other sulfide minerals occurs, particularly in sediments where anaerobic bacteria flourish (Ferris et al., 1989). The uranium may have been incidentally incorporated into the pyrite structure, although microbes are capable of sequestering uranium with their cells (Tebo and Obraztsova, 1998). The smaller framboids and clusters of pyrite octahedra are likely the result microbial deposition, but it is uncertain if the overgrowths are microbially mediated or if they have simply nucleated and grown on pre-existing pyrite under reducing conditions in the wood. The high concentration of uranium (130 μg/g) in the pyrite overgrowths is evidence that the uranium was sequestered into these late overgrowths after the contaminant plume had entered the sediment.

This Page Intentionally Left Blank

6. References

Bryan, C.R., Du Frane, S.A., Moir, D., Schloesslin, C., and Davis, K.M., 2003. *Selective Sequential Extraction Analysis of Uranium in Great Miami Aquifer Sediment Samples, Fernald DOE site, Ohio*, SAND2003-0192P, Sandia National Laboratories, Albuquerque, NM, 51 p.

Ferris, F.G., Shotyk, W., Fyfe, W.S., 1989. Mineral formation and decomposition by microorganisms. In Beveridge TJ and Doyle RJ (eds.) *Metal Ions and Bacteria,* 413-441.

Tebo, B. M.; Ghiorse, W. C., van Waasbergen, L. G., Siering, P. L., Caspi, R., 1997. Bacterially mediated mineral formation; insights into manganese(II) oxidation from molecular genetic and biochemical studies, In Banfield, J F; Nealson, K H (eds.) *Reviews in Mineralogy*, 35, 225-266.

Tebo, B.M., and Obraztsova, A.Y., 1998. Sulfate-reducing bacterium grows with Cr(VI), U(VI), Mn(IV),and Fe(III) as electron acceptors, *FEMS Microbiology Letters*, 162, 193-198.

This Page Intentionally Left Blank

Appendix A: Microanalytical Methods Used in this Study

Several microanalytical techniques were used to evaluate the distribution of uranium in the sediments. These include electron microprobe and scanning electron microscope (SEM) analysis; secondary ion mass spectrometry (SIMS); and high-resolution transmission electron microscope (HR-TEM) analysis. Detailed descriptions of these techniques, including sample preparation, instrument calibration, and analytical conditions, are presented below.

Sample Preparation for Microanalysis

In addition to the polished section provided (see Section 2), two polished sections were prepared at UNM for electron and ion microprobe analyses from sample KD33262 and were designated 33262A and 33262B. Unsorted sand from the sample container was mounted in epoxy, the surface ground flat with 240, 320 and 600 grit SiC paper, then polished with successive steps of 9, 6 and 3 µm diamond paste followed by 1, 0.3 and to 0.05 µm alumina slurry on rotating laps. For electron microprobe/SEM analysis, the polished sections were coated with approximately 20 nm of carbon evaporated onto the surface. Prior to SIMS (ion microprobe) analysis, the carbon coat was polished off and a 200 nm coat of gold was sputtered onto the surface.

Several loose pebbles from KD33262 were mounted for surface analysis by depth profiling in the ion microprobe. Four grains 3 to 6 mm in diameter and approximately 3 mm thick were cemented directly into a tantalum grid mount and then gold coated before analysis in the ion microprobe. After analysis, one pebble from this group and an additional pebble were cleaned in deionized water in an ultrasonic cleaner in order to remove any fine mineral material clinging to the surface. The two pebbles were then remounted on the ion microprobe grid for re-analysis.

Electron Microprobe Analysis and X-ray Mapping

The polished sections were analyzed using a JEOL 8200 electron microprobe at the Department of Earth and Planetary Science/Institute of Meteoritics, University of New Mexico. The microprobe is equipped with 5 wavelength dispersive x-ray spectrometers (WDS) and an ultrathin-window energy dispersive spectrometer (EDS). Point analyses were conducted at 15 kV and two different beam currents: 20 nA on silicates and 50 nA on pyrite. Uranium was measured on two spectrometers simultaneously, which allows the counting results to be added together, effectively doubling the count rate and increasing analytical sensitivity. For each spectrometer, U was counted for 300 seconds on the peak and 50 seconds on two background positions above and below the analytical x-ray peak. The 2σ detection limit (95% confidence level) was 92 µg/g U (105 µg/g UO_2) on silicates and 80 µg/g U on pyrite; the 3σ detection limit (99% confidence level) was 138 µg/g U (156 µg/g UO_2) and 120 µg/g U, respectively. Counting times on other elements were 20 seconds for major elements and 30 seconds for minor elements. Natural mineral standards were used as calibration standards except for a pure U-metal. A ZAF correction program from JEOL was used to reduce the raw data. Table A-1 contains analyses on a pyrite standard as a check of the instrument calibration, with a comparison to the expected standard values. All of the uranium results on the pyrite standard are below the 2σ detection limit, as would be expected for a pure pyrite.

Table A-1. Analyses of Taylor pyrite standard and expected values, wt.%.

No.	Fe	S	U*	Total
6	46.024	53.701	0.005	99.73
17	45.781	54.4	0.007	100.188
18	45.876	54.625	0.005	100.506
Std value	46	54	0.0	100

*2σ detection limit = 0.0092 Wt% U

X-ray maps utilized several different working configurations. Maps on silicate minerals were done at 15 kV and 50 nA, and pyrite maps were collected at 20 kV and either 20 or 50 nA. Wavelength dispersive mapping was used to map Al, Fe, U, and the U-background (measured at the indium spectral position); Mg, Si, S, and Ca were mapped by EDS. After installation of a high sensitivity spectrometer, Mg, Al, Fe, Ca, and U were all done by WDS with Si and S by EDS. The new spectrometer and software allowed WDS backgrounds to be collected in sequence with the elements, and thus the indium position was no longer used as a background for subsequent maps. Map acquisition time was 12-15 hrs including backgrounds for all but one map on the polished section KD33262, in which case, the map acquisition time was 30.5 hours.

Ion Microprobe Analysis

Trace element analysis of the polished sections was conducted by secondary ion mass spectrometry (SIMS) on a Cameca IMS 4f ion microprobe at the Department of Earth and Planetary Science/Institute of Meteoritics, University of New Mexico. Two analytical approaches were used in the analysis of individual grains and grain coatings: standard quantitative analysis and depth profiling. Standard analysis of mineral grains and coatings included measuring ^{30}Si and ^{44}Ca, and ^{238}U. Analyses were made by bombarding the sample with primary O^- ions at a nominal potential of 10 kV. A primary ion current of 15 nA was focused on the sample to a spot diameter of 10-15 μm. Sputtered secondary ions were energy filtered using a sample-offset voltage of 105 V, and an energy window of ±25 V, to eliminate isobaric interferences. Peak counting times were 2 seconds on ^{30}Si and ^{44}Ca and 10 seconds on ^{238}U. Absolute concentrations of U were calculated using empirical relationships of measured peak/^{30}Si ratios normalized to known SiO_2 content from EMP and measured peak/^{44}Ca ratios normalized to known CaO content from EMP analyses for carbonates. NBS 610 standard was used to construct the U calibration curve. Table A-2 provides the results for both silicate and carbonate calibration. The 2σ detection limit is approximately 0.2 μg/g for uranium.

The ion microprobe offers the unique capability of depth profiling, the capability to mill into the sample, ion by ion, while recording the change in concentration of elements of interest. Depth profiling for U, Si. Al and Ca (and Fe in some instances) was done on the raw surfaces of pebbles to record any changes in U concentration from the surface to some depth into the rock. Whole pebbles were mounted in the SIMS grid holder, gold coated, and placed in the ion microprobe. Several areas were analyzed on each pebble. Depth profiling was accomplished by rastering a primary O^- beam over an area of approximately

5634

Table A-2. Silicate and carbonate calibration data for uranium.

Silicate Standardization Standard	Intensity	Conc.	Counting Time	Intensity (Counting Time Corrected)	Conc.
NBS610	1.88353	460	10	1.88353	460
NBS612	0.14765	37.4	10	0.14765	37.4
NBS610-2	2.02443	460	10	2.02443	460
NBS614	0.00884	0.8	20	0.00442	0.8

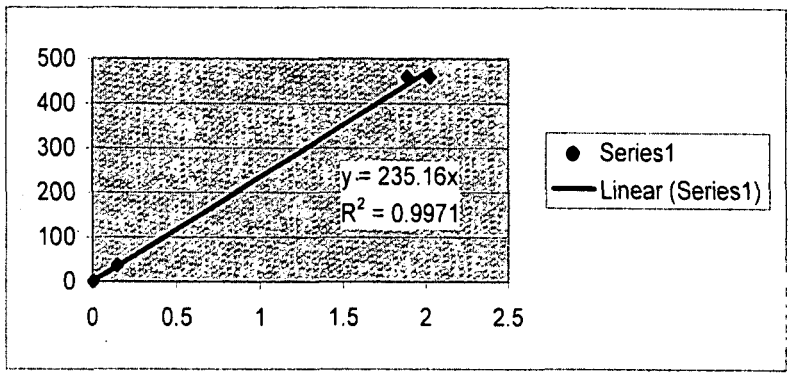

Carbonate Standardization Standard	Intensity	Conc.	Counting Time	Intensity (Counting Time Corrected)	Conc.
NBS610	3.72578	460	10	3.72578	460
NBS612	0.26424	37.4	10	0.26424	37.4
NBS610-2	3.38986	460	10	3.38986	460
NBS614	0.01557	0.8	20	0.00778	0.8

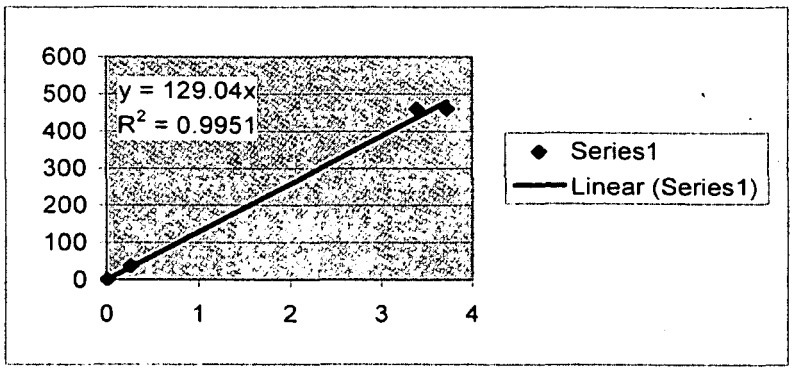

150 microns by 150 microns. The primary ions were accelerated at a nominal potential of 10 kV and a primary ion current of between 8 and 15 nA. The variation in current resulted in a change in depth resolution and intensity. A 40 micron aperture was used to sample ions from the flat portion of the rastered crater. Sputtered secondary ions were energy filtered using a sample offset voltage of 105 V, and an energy window of ±25 V, to eliminate isobaric interferences. Peak counting times of 2 seconds were used for ^{30}Si, ^{27}Al, ^{44}Ca, and ^{56}Fe, and 10 seconds for ^{238}U. Each element is analyzed sequentially for the chosen analysis time, and then the cycle repeats. The number of cycles for each profile was adjusted to efficiently produce relevant data. Silicon, Al, Ca, and Fe were not run on every profile.

Profiling depth must be determined by independent means after analysis, and on smooth (artificial) surfaces this is done with a profilometer. However on these natural samples, it was impossible to determine the actual final sampling depth either by mechanical means or by SEM observation. The ion milling process resulted in a highly irregular final surface, intensifying the initial surface roughness of the pebble.

Scanning Electron Microscopy (SEM)

Before and after depth profiling in the SIMS, sample pebbles were imaged in the scanning electron microscope, first to determine the type of minerals present, and after to observe the ion excavated pit. Imaging and EDS qualitative analysis was carried out on a JEOL JSM5800LV Scanning Electron Microscope at the University of New Mexico, Department of Earth and Planetary Science/Institute of Meteoritics. The SEM is equipped with an Oxford Instruments thin-window EDS and an Oxford X-ray analyzer. Accelerating voltage was 20 kV, with a beam current of less than 0.5 nA and a spot size of less than 1 μm.

TEM analysis

Characterization of fine particles, grain coatings, and grain edges in the contaminated sediment (borehole KD33262, depth interval 52.75'–53.75') was done at the Transmission Electron Microscopy Lab, University of New Mexico using JEOL 2010 and JEOL 2010F (a point-to-point resolution of 0.19 nm) microscopes with an Oxford Instruments Link ISIS EDS system, operated at 200 KV. Beam diameter in the EDS analyses ranged from 10 to 100 nm, depending on the spot analysis requirements. The <2 μm fraction was separated by sedimentation, and prepared for TEM observations by mixing the collected particles and isopropyl alcohol between two glass slides. A drop of the resulting suspension was placed onto holly carbon film supported by a copper TEM grid and air-dried. To measure coating materials on coarser grains, grains were gently washed and abraded, and the fine material released during the process was mounted in a similar fashion as above. Some sediment grains and wood fragments from the second sample (borehole KD33298, depth interval 66.0'–66.5') were fixed using epoxy, cut using an ultra-microtome, and the resulting thin slices were placed on a Cu grid for TEM analysis.

5631

Appendix B: Chemical Composition of Groundwater Samples collected during the Batch Sorption/Desorption Experiments

Filtered solution samples were collected periodically during the batch sorption/desorption experiments. Following collection, each groundwater sample was transferred to a plastic bottle, acidified and diluted, and stored for analysis by Inductively-Coupled-Plasma Mass Spectrometry. Blanks and duplicates were run to evaluate precision and reproducibility—for more detailed information, see the Carlsbad Environmental Monitoring & Research Center data package. In addition to uranium, the water samples were analyzed for Al, Fe, Mn, Mg, Ca, Na, and K to monitor potential changes in water chemistry due to mineral precipitation/dissolution or ion exchange.

Table B-1 Summary of Chemical Analyses of Sorption Experiment Solution Samples

	Days Elapsed	Sample size, mL	Concentration, µg/L						
			U	Ca	Fe	K	Mg	Mn	Na
A-2									
Set 1 Spiked with 80 µg/L U	1	0.50	327.8	112942	195	7077	29670	19	19212
	2	0.50	316.8	118217	648	6974	28856	29	20804
	5	0.50	294.6	119045	1307	7230	30335	46	21074
	8	0.50	270.4	114437	751	7933	30282	30	25393
	11	0.50	244.9	102105	1645	7961	28837	44	24826
	14	0.50	235.9	103747	1421	9594	30612	39	26243
	17	0.50	192.7	104902	7365	9188	32704	168	26632
	21	2.13	182.8	115493	4905	11114	34498	83	29724
Set 2 Spiked with 30 µg/L U	1	0.50	312.2	91761	1876	7356	29541	53	23271
	2	0.50	279.4	81153	1122	9574	25564	43	22993
	5	0.50	200.7	73116	694	7171	21522	20	17141
	8	0.50	191.1	76220	1182	7239	22673	29	18337
	11	0.50	179.8	85565	9026	9806	26168	158	20284
	14	0.50	164.1	77674	332	8010	23269	17	20786
	17	0.50	168.9	79783	494	8177	24153	19	21109
	21	1.69	151.4	82656	739	9212	25489	28	22959
Set 3 Spiked with 20 µg/L U	1	0.50	225.5	72508	206	6822	23376	18	15676
	2	0.50	213.1	81507	1309	7682	24077	52	16646
	5	0.50	184.0	70265	2809	8409	27275	59	21911
	8	0.50	181.8	59983	1070	8850	25825	24	23519
	11	0.50	166.4	62359	5832	8798	26381	106	24032
	14	0.50	157.2	55051	269	8827	24982	12	24028
	17	0.50	125.5	55115	356	8933	24398	13	25540
	21	1.87	130.5	57574	162	8976	26290	13	25909

Table B-1 Continued.

	Days Elapsed	Sample size, mL	Concentration, µg/L						
			U	Ca	Fe	K	Mg	Mn	Na
Ab-1									
Set 1	1	0.50	371.8	121306	162	6911	30317	15	21268
	2	0.50	312.9	104864	806	7087	29336	31	20277
	5	0.50	301.4	114765	6291	6314	28500	143	21058
	8	0.50	263.8	99581	893	7336	27798	26	23714
	11	0.50	253.7	120658	14649	11850	33914	284	24778
	14	0.50	241.3	119447	14522	12622	34818	310	25634
	17	0.50	158.0	108346	15099	9814	31437	327	25689
	21	2.35	118.5	103717	11269	12301	31252	183	26826
Set 2	1	0.50	304.6	88647	1312	7207	27567	44	22904
	2	0.50	243.0	81717	1531	7455	25200	34	21939
	5	0.50	197.6	86711	11145	8510	24769	198	16727
	8	0.50	188.2	74857	1644	7459	23082	38	18738
	11	0.50	174.9	77184	6579	9118	24298	104	24367
	14	0.50	166.8	76233	742	7711	23580	23	20499
	17	0.50	168.5	84126	4786	9038	25502	86	21412
	21	1.74	119.3	84008	891	10130	24411	29	27744
Set 3	1	0.50	226.6	78093	2210	6928	23640	66	16444
	2	0.50	198.8	84581	7620	9407	26668	169	16764
	5	0.50	176.3	58023	1187	8064	24653	25	23808
	8	0.50	174.7	55901	1579	7521	24390	32	20783
	11	0.50	163.6	61450	4485	8417	25884	79	22068
	14	0.50	129.4	50874	198	7674	23523	12	22605
	17	0.50	99.6	53909	3488	8758	24212	73	23782
	21	1.49	91.6	52684	162	7755	21271	5	23084
Ab-2									
Set 1	1	7.18	365.5	118696	197	7036	30818	18	21087
	2	7.03	317.1	118759	1155	7248	28540	42	27753
	5	6.92	377.6	92662	1260	6014	24066	46	16208
	8	6.26	332.9	92359	2830	7157	26828	69	19097
	11	5.83	310.5	86748	508	5619	26435	23	17511
	14	5.87	263.1	78723	732	5646	25217	26	16722
	17	5.41	218.2	74704	1868	6083	25825	47	17644
	21	5.94	303.9	88244	607	5749	29584	25	18618
Set 2	5	6.79	274.5	77013	506	5601	26411	23	12970
	11	6.28	250.7	88107	3014	6236	29080	60	13686
	17	5.99	212.7	78943	396	5596	26636	23	14559
	21	5.81	178.2	77349	1035	5229	24971	31	13729
Set 3	5	6.87	189.8	64819	860	5999	28769	26	17006
	11	6.72	182.7	72045	4606	5779	31465	88	16655
	17	6.46	167.8	62804	443	5601	27451	20	15263

Table B-1 Continued.

	Days Elapsed	Sample size, mL	Concentration, µg/L						
			U	Ca	Fe	K	Mg	Mn	Na
B-1									
Set 1 Spiked with 80 µg/L U	1	0.50	376.0	125867	2117	6915	31950	65	20286
	5	0.50	362.1	148375	5176	6991	38346	151	21481
	11	0.50	320.0	112924	2201	7027	30981	56	23016
	17	4.92	264.5	112409	1348	7269	30342	43	26887
Set 2 Spiked with 30 µg/L U	1	0.50	342.6	86467	1266	5976	25898	31	19968
	5	0.50	271.1	80968	759	5828	22743	21	15353
	11	0.50	239.6	82709	1008	5541	21832	34	17953
	17	0.50	244.3	77691	253	5779	21704	22	15517
	21	4.21	247.8	80829	608	6328	22841	28	17449
Set 3 Spiked with 20 µg/L U	1	0.50	256.2	73184	867	5899	23085	30	14755
	5	0.50	247.3	68778	2563	6152	24760	52	11293
	11	0.50	248.9	58617	997	6322	25025	23	17584
	17	4.71	244.3	54145	884	6125	24047	22	17467
B-2									
Set 1 Spiked with 80 µg/L U	1	0.50	387.1	123845	2111	8012	30801	57	19853
	5	0.50	372.7	128744	3307	6980	33062	101	20868
	11	0.50	335.1	108479	1923	7143	30158	50	22432
	17	4.65	267.1	108902	434	7112	29635	21	25345
Set 2 Spiked with 30 µg/L U	1	0.50	314.2	95436	3344	6601	28328	93	20863
	5	0.50	263.5	81982	793	6175	22240	23	14528
	11	0.50	230.3	79940	394	5847	22419	20	15550
	17	0.50	224.3	76249	125	5742	21721	17	15800
	21	3.76	170.1	70803	575	6175	19799	24	15777
Set 3 Spiked with 20 µg/L U	1	0.50	242.0	77303	1510	6184	24442	50	13972
	5	0.50	237.4	54265	811	6340	22617	14	17043
	11	0.50	228.3	52698	1378	5983	22099	32	16476
	17	4.30	187.5	68174	762	5814	21033	23	17141

Table B-1 Continued.

	Days Elapsed	Sample size, mL	Concentration, µg/L						
			U	Ca	Fe	K	Mg	Mn	Na
Bb-1									
Set 1	1	0.50	406.6	109114	537	6945	27989	23	19527
	5	0.50	357.9	108978	2133	6722	27726	68	20061
	11	0.50	318.9	117417	8907	8808	32850	203	23170
	17	4.68	256.3	96943	1096	7079	28321	34	22937
Set 2	1	0.50	302.7	78622	1012	6760	25238	30	19629
	5	0.50	259.3	78322	1143	6269	22470	28	15714
	11	0.50	198.3	73142	1232	5610	20279	32	14952
	17	0.50	188.1	72018	421	5447	20883	20	15877
	21	4.60	191.7	74434	1253	6244	20292	41	16250
Set 3	1	0.50	232.8	71221	1007	5890	22751	35	14015
	5	0.50	190.0	56383	2248	6054	21477	38	16281
	11	0.50	182.1	64560	3831	6217	27795	74	16990
	17	4.28	166.1	47419	894	6057	21375	18	17404
Bb-2									
Set 1	1	7.13	390.7	109031	830	7027	27589	30	19466
	5	7.19	408.8	121203	5734	6224	32576	154	16750
	11	6.66	379.1	86770	1926	6167	25409	43	17666
	17	6.47	299.3	87881	1449	5879	26535	44	17781
Set 2	5	6.86	284.0	82875	1032	5399	23966	28	13730
	11	6.44	256.2	77386	126	4872	23534	15	13165
	17	5.95	222.0	73640	21	4330	22350	15	12408
	21	6.06	225.5	79598	1311	5161	23984	46	13774
Set 3	5	6.78	208.1	59987	1358	5200	25358	25	14953
	11	6.91	208.9	56853	1123	4898	26024	22	14369
	17	6.71	191.6	50150	596	4972	25790	15	14989

5634

Table B-1 Continued.

	Days Elapsed	Sample size, mL	Concentration, µg/L						
			U	Ca	Fe	K	Mg	Mn	Na
C-1									
Set 1 Spiked with 80 µg/L U	11	0.50	420.3	117756	1606	6864	32711	53	22815
	21	6.51	354.9	116021	1755	7034	32789	54	23962
Set 2 Spiked with 30 µg/L U	11	0.50	298.2	77340	697	4911	21335	25	13231
	21	6.15	282.9	80429	388	5529	22436	22	14635
Set 3 Spiked with 20 µg/L U	11	0.50	276.8	52548	754	5215	23056	15	15315
	21	6.14	274.8	72992	3027	5715	29089	82	16398
C-2									
Set 1 Spiked with 80 µg/L U	11	0.50	440.7	120212	1613	6897	32664	54	24411
	21	6.47	370.5	121107	2776	7381	34200	70	24420
Set 2 Spiked with 30 µg/L U	11	0.50	348.8	97146	2827	5256	26483	67	14685
	21	6.16	296.9	78983	110	5539	22066	14	15879
Set 3 Spiked with 20 µg/L U	11	0.50	278.4	50586	859	5665	23847	17	16007
	21	6.13	273.1	51085	611	6371	23400	16	15991

Table B-1 Continued.

	Days Elapsed	Sample size, mL	Concentration, µg/L						
			U	Ca	Fe	K	Mg	Mn	Na
Cb-1									
Set 1	11	0.50	441.1	111204	1162	6234	31260	45	21693
	21	6.24	367.2	117423	5333	8717	32973	121	24496
Set 2	11	0.50	336.7	88204	906	5484	24176	36	14713
	21	6.08	269.5	80310	301	8123	21960	26	14667
Set 3	11	0.50	250.6	58954	604	4991	22057	17	15333
	21	6.15	203.1	48431	1120	4538	19585	30	13901
Cb-2									
Set 1	11	7.16	431.8	122632	2398	6697	33303	81	22317
	21	6.68	357.8	94563	2281	6722	27735	64	19348
Set 2	11	7.00	325.7	93370	2335	5256	25629	58	13467
	21	6.10	268.7	91746	1558	5370	25266	56	16026
Set 3	11	6.75	226.4	71375	4168	5282	30051	92	14900
	21	6.98	194.8	50534	435	4509	22068	16	13391